On superelastic bending of shape memory alloy beams

Reza Mirzaeifar [a], Reginald DesRoches [b], Arash Yavari [a,b,*], Ken Gall [a,c]

[a] George W. Woodruff School of Mechanical Engineering, Georgia Institute of Technology, Atlanta, GA 30332, USA
[b] School of Civil and Environmental Engineering, Georgia Institute of Technology, Atlanta, GA 30332, USA
[c] School of Materials Science and Engineering, Georgia Institute of Technology, Atlanta, GA 30332, USA

ARTICLE INFO

ABSTRACT

In this paper, a closed-form solution is presented for bending analysis of shape memory alloy (SMA) beams. Two different transformation functions are considered: a J_2-based model with symmetric tension–compression response, and a J_2-I_1-based model for considering the tension–compression asymmetry that is observed in experiments. The constitutive equations are reduced to an appropriate form for studying the pseudoelastic bending response of SMAs. Closed-form expressions are given for the stress and martensitic volume fraction distributions in the cross section and the bending moment–curvature relation is obtained analytically. Both circular and rectangular cross sections are considered and several case studies are presented for testing the accuracy of the method and also the effect of taking into account the tension–compression asymmetry on the bending response of SMAs. The results of a three-point bending test on an SMA beam are presented and compared with the theoretical predictions. Using some experimental data on bending of a nickel–titanium micropillar the applicability of the present method in the micro scale is studied. It is shown that this method can be used for assessing the tensile properties of materials in this special case, where the compressive and bending responses are known from experiments while the tensile properties are very difficult to be measured experimentally.

© 2013 Elsevier Ltd. All rights reserved.

1. Introduction

Mirzaeifar et al. (2010, 2011c,b) recently developed analytic and semi-analytic methods for simulating the pseudoelastic response of various shape memory alloy (SMA) devices subjected to different loading conditions. In many SMA devices, the SMA instrument is subjected to local or global bending. This is the main motivation for several reported works on bending analysis of SMAs in the literature. The bending of beams made of single crystal SMAs and the propagation of phase boundaries was studied by Purohit and Bhattacharya (2002). They used additional kinetic relations in conjunction with the constitutive assumptions and balance laws to determine the propagation of phase boundaries. The solutions for single crystalline beams consider a jump in the material properties before and after the phase transformation, and there is no intermediate condition between these two cases. In polycrystalline materials, which are used in the majority of SMA engineering applications, the phase transformation does not occur simultaneously in all the grains. This causes a considerable difference between the material properties in single crystals and polycrystalline samples. While the material in a beam made of a single crystal SMA is austenite or martensite with some phase boundaries, the

continuous change of material properties in polycrystalline SMAs makes modeling the bending of beams made of these materials a challenging problem (see Thamburaja and Anand (2001, 2002) and Anand and Gurtin (2003) for studying polycrystalline SMAs using a constitutive model based on the response of single crystal SMAs).

Among the solutions available for modeling bending in polycrystallline SMAs a large number are purely numerical (Auricchio and Sacco, 1999; Marfia et al., 2003). In an early work, Atanackovic and Achenbach (1989) used a simplified multi-linear constitutive equation for obtaining the moment–curvature relation of a pseudoelastic beam. Plietsch et al. (1994) presented a closed-form solution for bending of SMA beams by considering a multi-linear stress–strain response. Auricchio and Sacco (2001) studied the SMA wires subjected to cyclic stretching-bending loads using a one-dimensional constitutive model. In their work the thermo-mechanical coupling was also considered and the finite element method was used for solving the governing equations. Auricchio et al. (2011) implemented one-dimensional constitutive equations into a finite element model for studying the shape memory effect for SMA beams in bending. The material response in tension and compression was assumed asymmetric and the numerical results were compared with experiments. Recently, Flor et al. (2011) presented some numerical simulation and experimental analysis of SMA wires in bending. They considered tension–compression asymmetry in their model and a numerical scheme was used for calculating

---

* Corresponding author at: School of Civil and Environmental Engineering, Georgia Institute of Technology, Atlanta, GA 30332, USA. Tel.: +1 404 894 2436.
E-mail address: arash.yavari@ce.gatech.edu (A. Yavari).

the bending response. Their model is developed only for the loading phase; unloading was not studied in either their experiments or numerical simulations.

The existing numerical methods suffer from the high computational cost and convergence difficulties particularly for modeling the unloading process or considering the geometric nonlinearities. The results obtained using these numerical methods are highly sensitive to a large number of secondary parameters, e.g. the mesh size, tolerance criteria, and number of loading steps. The numerical simulations may give erroneous results due to an improper choice for any of these parameters. On the other hand, the semi-analytic solutions in the literature are based on oversimplified constitutive relations or using unrealistic simplifying assumptions. In this paper, we introduce a closed-form solution for analyzing the superelastic bending of shape memory alloys. A three-dimensional constitutive model is reduced to an appropriate one-dimensional constitutive equation. Closed-form expressions are obtained for the martensitic volume fraction and stress distributions in the cross section of SMA beams in bending. The Euler–Bernoulli beam theory (assuming the plane cross sections remain plane and perpendicular to the centerline after deformation) is used and the bending moment–curvature relation is obtained analytically. A method is presented for solving the bending of superelastic SMAs analytically. In addition to the J_2-based model that predicts a symmetric response in tension and compression, a more accurate solution based on J_2-I_1 transformation function is also presented and the effect of considering the tension–compression asymmetry (which is a well-known response for most SMAs (Gall et al., 1999a; Anand and Gurtin, 2003)) in the bending response is studied.

It is worth noting that for modeling the tension–compression asymmetry, the J_2-J_3 model gives more accurate results because of its capability in modeling the negative volume change during martensitic transformation (Qidwai and Lagoudas, 2000b). However, the J_2-J_3-based model cannot be used for developing a closed-form solution in this paper. Experiments have shown that the J_2-I_1-based model can predict the superelastic response of SMAs with a good accuracy for all the parameters except the volumetric transformation strain (see Section 4 in Qidwai and Lagoudas (2000b)). Also, the material parameters in the J_2-I_1-based model can be calibrated for modeling a realistic volumetric transformation strain, but in this case the tension–compression asymmetry is not modeled correctly. We will not use this calibration method in our solution.

An important capability of our model is its applicability in extracting the tensile properties of materials when the compression and bending test results are available but the tension properties are practically difficult to be measured experimentally, e.g. in the micro scale applications of SMAs.

SMAs have recently attracted considerable interest for applications as actuators in micro-electro-mechanical systems (MEMS) (Kahn et al., 1998; Bhattacharya et al., 2005; Shin et al., 2005) due to their relatively high work output per unit volume (Krulevitch et al., 1996). One of the traditional methods for studying the mechanical properties of a material in the micro and nano scales is testing pillars. These pillars are produced by focused ion beam (FIB) micromachining (Volkert and Minor, 2007). Recently, the pseudoelasticity, crystal orientation effect, and size dependency have been extensively studied experimentally for nickel–titanium and Cu–Al–Ni micropillars (Frick et al., 2007; Juan et al., 2008, 2009; Manjeri et al., 2010; Clark et al., 2010). In order to have a precise description of the micropillars response in MEMS applications, it is ideal to extract the material response in tension, compression, and bending experimentally. However, among the reported works on studying the shape memory micropillars response the majority of experiments are performed for compressive loading (Frick et al., 2007; Juan et al., 2008, 2009; Manjeri et al., 2010); there are very few experimental works on bending (Clark et al., 2010).

While performing bending tests on micropillars one faces some technical difficulties (Clark et al., 2010). Tensile tests in the nano and micro scales are considerably more difficult because a special geometric shape should be created at the pillar head for attaching the tensile tool to the pillar (Kim et al., 2009; Kim and Greer, 2009). As we explain in Section 4.6, our analytical solution for bending can be used for extracting the tensile properties when the bending and compressive responses are known.

The material properties in compression are calibrated from the available experimental data. The material-independent properties in tension are assumed and bending is simulated using these properties in tension and compression. The predicted bending response is compared with the experimental data and a trial and error approach is used for improving the assumed tensile material properties for finding the best match between the experimental and analytical results. It is worth noting that the iterations for improving the initial guess are performed without a considerable computational cost; the closed-form solutions are obtained in a few seconds. Such a method is extremely time consuming if the available numerical solutions are used for modeling the bending response. In the numerical results section, we will implement this method for analyzing bending of a nickel–titanium micropillar using the available experimental data.

This paper is organized as follows. In Section 2 a general three-dimensional constitutive equation for polycrystalline SMAs using two different transformation functions and an appropriate reduced constitutive equation for pure bending are discussed. In this section explicit expressions are given for the stress and martensitic volume fraction distributions as functions of the curvature in bending. In Section 3, these explicit expressions are used and three different analytic approximations for the relation between the bending moment and curvature are presented. Numerical results for macroscale SMA beams with circular and rectangular cross sections are given in Section 4. The results of a three-point bending test are presented and compared with the theoretical results in Section 4.5. The available experimental data on bending of a NiTi micropillar are used for studying the applicability of our method for modeling this problem in Section 4.6. Conclusions are given in Section 5.

2. Three-dimensional constitutive equations and one-dimensional reduction for bending

We use the three-dimensional phenomenological macroscopic constitutive model for polycrystalline SMAs proposed by Boyd and Lagoudas (1996). In this constitutive model, by considering the transformation strain ϵ^t (the portion of strain that is recovered due to reverse phase transformation from detwinned martensite to austenite) and the martensitic volume fraction ξ (an indicator of the extent of the phase transformation from austenite to martensite) as the internal state variables, the following expression is obtained for the Gibbs free energy potential (Qidwai and Lagoudas, 2000b):

$$G(\boldsymbol{\sigma}, T, \boldsymbol{\epsilon}^t, \xi) = -\frac{1}{2\rho}\boldsymbol{\sigma} : \mathbb{S} : \boldsymbol{\sigma} - \frac{1}{\rho}\boldsymbol{\sigma} : \left[\boldsymbol{\alpha}(T - T_0) + \boldsymbol{\epsilon}^t\right]$$
$$+ c\left[(T - T_0) - T \ln\left(\frac{T}{T_0}\right)\right] - s_0 T + u_0 + \frac{1}{\rho}f(\xi), \quad (1)$$

where, $\mathbb{S}, \boldsymbol{\alpha}, c, \rho, s_0$ and u_0 are the effective compliance tensor, effective thermal expansion coefficient tensor, effective specific heat, mass density, effective specific entropy, and effective specific internal energy at the reference state, respectively. The symbols $\boldsymbol{\sigma}, T, T_0, \boldsymbol{\epsilon}^t$, and ξ denote the Cauchy stress tensor, temperature, reference temperature, transformation strain, and martensitic volume fraction, respectively. Any effective material property $\mathbf{P}$ is assumed to vary with the martensitic volume fraction as $\mathbf{P} = \mathbf{P}^A + \xi \Delta \mathbf{P}$, where the superscript A denotes the austenite phase and the symbol $\Delta(\cdot)$

denotes the difference of a quality $(\cdot)$ between the martensitic and austenitic phases, i.e. $\Delta(\cdot) = (\cdot)^M - (\cdot)^A$ with M denoting the martensite phase.

In (1), $f(\xi)$ is a hardening function that models the transformation strain hardening in the SMA material. In the Boyd–Lagoudas polynomial hardening model (Lagoudas, 2008), this function is given by

$$f(\xi) = \begin{cases} \frac{1}{2}\rho b^M \xi^2 + (\mu_1 + \mu_2)\xi, & \dot{\xi} > 0, \\ \frac{1}{2}\rho b^A \xi^2 + (\mu_1 - \mu_2)\xi, & \dot{\xi} < 0, \end{cases} \quad (2)$$

where, $\rho b^A, \rho b^M, \mu_1$ and μ_2 are material constants for transformation strain hardening. The first condition in (2) represents the forward phase transformation $(A \to M)$ and the second condition represents the reverse phase transformation $(M \to A)$. The constitutive relation of a shape memory material can be obtained by using the total Gibbs free energy as

$$\epsilon = -\rho\frac{\partial G}{\partial \boldsymbol{\sigma}} = \mathbb{S} : \boldsymbol{\sigma} + \boldsymbol{\alpha}(T - T_0) + \boldsymbol{\epsilon}^t, \quad (3)$$

where ϵ is the strain tensor. By introducing a generalized thermodynamic force $\mathcal{P}$ as:

$$\mathcal{P} = -\rho\frac{\partial G}{\partial \xi} = \frac{1}{2}\boldsymbol{\sigma} : \Delta\mathbb{S} : \boldsymbol{\sigma} + \Delta\boldsymbol{\alpha} : \boldsymbol{\sigma}(T - T_0)$$
$$+ \rho\Delta c\left[(T - T_0) - T\ln\left(\frac{T}{T_0}\right)\right] + \rho\Delta s_0 T - \frac{\partial f}{\partial \xi} - \rho\Delta u_0, \quad (4)$$

the second law of thermodynamics in the form of non-negativeness of the rate of entropy production density can be expressed as $\boldsymbol{\sigma} : \dot{\boldsymbol{\epsilon}}^t + \mathcal{P}\dot{\xi} = \pi\dot{\xi} \geqslant 0$ (Mirzaeifar et al., 2011a). We assume the existence of a thermo-elastic region (transformation surface) bounded by a smooth hypersurface, which can be described by a transformation function Φ as $\Phi(\boldsymbol{\sigma}, \mathcal{P}) = 0$. We choose the following general form for the transformation function (Qidwai and Lagoudas, 2000b)

$$\Phi(\boldsymbol{\sigma}, \mathcal{P}) = \left[\tilde{\Phi}(\boldsymbol{\sigma}) + \mathcal{P}\right]^2 - Y^2$$
$$= \left[\tilde{\Phi}(\boldsymbol{\sigma}) + \mathcal{P} + Y\right]\left[\tilde{\Phi}(\boldsymbol{\sigma}) + \mathcal{P} - Y\right], \quad (5)$$

where $\tilde{\Phi}(\boldsymbol{\sigma})$ is the stress related transformation function that will be defined in the following sections and Y is a measure of internal dissipation due to microstructural changes during phase transformation. The transformation surface that controls the onset of direct (austenite to martensite) and reverse (martensite to austenite) phase transformation is defined as

$$\tilde{\Phi}(\boldsymbol{\sigma}) + \mathcal{P} = \begin{cases} Y, & \dot{\xi} > 0, \\ -Y, & \dot{\xi} < 0. \end{cases} \quad (6)$$

Considering the fact that any change in the state of the system is only possible by a change in the internal state variable ξ (Bo and Lagoudas, 1999), the evolution of the transformation strain tensor is related to the evolution of the martensitic volume fraction as $\dot{\boldsymbol{\epsilon}}^t = (\partial\tilde{\Phi}(\boldsymbol{\sigma})/\partial\boldsymbol{\sigma})\dot{\xi} = \boldsymbol{\Gamma}\dot{\xi}$, where $\boldsymbol{\Gamma}$ represents a transformation tensor associated with the chosen transformation function.

By ignoring the shear force in the cross section of an SMA beam subjected to bending, the state of stress and strain is one dimensional. Considering the cross section in the yz-plane and the beam axis along the x-axis, the only non-zero stress component is σ_x. However, the strain and transformation strain tensors have other non-zero components as will be shown in the following two sections where the transformation tensor is obtained.

2.1. Transformation function based on J_2 with symmetric tension–compression response

By an appropriate selection of the function $\tilde{\Phi}(\boldsymbol{\sigma})$, different material responses observed in experiments can be modeled by this constitutive framework. There are numerous selections for the transformation function of SMAs in the literature based on J_2 (Qidwai and Lagoudas, 2000a), J_2-J_3 (Gillet et al., 1998), J_2-I_1 (Auricchio et al., 1997), and $J_2-J_3-I_1$ (Qidwai and Lagoudas, 2000b). The models with a transformation function based on a J_2 invariant are the simplest and the best choice for our purposes of seeking a closed-form solution. However, by developing the constitutive equations based on J_2 invariant, although the majority of the SMA experimentally-observed responses are modeled with good accuracy, the tension–compression asymmetry (that plays an important rule in bending as will be shown in the numerical results section) cannot be modeled. We will use a J_2-based model and also modify it by using a J_2-I_1 model for taking into account the tension–compression asymmetry. The function $\tilde{\Phi}(\boldsymbol{\sigma})$ for a J_2-invariant based model is given by

$$\tilde{\Phi}(\boldsymbol{\sigma}) = \aleph\sqrt{3J_2} = \aleph\sqrt{\frac{3}{2}\boldsymbol{\sigma}' : \boldsymbol{\sigma}'}, \quad (7)$$

where $\aleph$ is a material constant corresponding to the maximum transformation strain during forward phase transformation in tension or compression. In (7) the deviatoric stress is $\boldsymbol{\sigma}' = \boldsymbol{\sigma} - \frac{1}{3}(\text{tr}\boldsymbol{\sigma})\mathbf{I}$, where $\mathbf{I}$ is the identity matrix. The transformation tensor associated with this function is obtained as $\boldsymbol{\Gamma} = \frac{3\aleph}{2}\frac{\boldsymbol{\sigma}'}{\sqrt{3J_2}}$ (Mirzaeifar et al., 2011a). The evolution equation in this case reads $\dot{\boldsymbol{\epsilon}}^t = \boldsymbol{\Gamma}\dot{\xi}$.

For studying pure bending in SMAs knowing that the only non-zero stress component is σ_x, the second deviatoric stress invariant is simplified and $\sqrt{3J_2} = |\sigma_x|$. The transformation tensor for pure bending in the case of J_2-based model is reduced to read

$$\boldsymbol{\Gamma} = \aleph\,\text{sgn}(\sigma_x)\begin{bmatrix} 1 & 0 & 0 \\ 0 & -0.5 & 0 \\ 0 & 0 & -0.5 \end{bmatrix}, \quad (8)$$

where $\text{sgn}(\cdot)$ is the sign function. Substituting (8) into the evolution equation, if we denote the transformation strain along the beam axis by ϵ_x^t, the transformation strain components in the cross section are $\epsilon_y^t = \epsilon_z^t = -0.5\epsilon_x^t$ and the other components are zero during loading. This is equivalent to assuming that phase transformation is an isochoric (volume preserving) process, which is a consequent of considering the transformation function based only on the J_2-invariant. It is worth noting that in developing the three-dimensional constitutive relations a more precise model is obtained by assuming a different transformation tensor related to the second deviatoric transformation strain invariant during reverse phase transformation (Mirzaeifar et al., 2010, 2011a), but in the present case of pure bending in which the normal stress is the only non-zero stress component, the transformation tensors are identical during forward and reverse phase transformations.

2.2. Modeling tension–compression asymmetry using a J_2-I_1-based transformation function

It is experimentally well known that single crystal and polycrystalline shape memory alloys have a non-symmetric tension–compression response (Liu et al., 1998; Gall et al., 1999b, 2001; Thamburaja and Anand, 2001). There have been numerous efforts in the literature for better understanding the origins of this secondary effect in SMAs and introducing appropriate constitutive relations capable of modeling this effect (Patoor et al., 1995; Paiva et al., 2005; Auricchio et al., 2009). Most of the existing constitutive

relations for modeling the tension–compression asymmetry are appropriate only for numerical simulations and not for closed-form solutions because of their complexity. We use the J_2-I_1-based transformation function that enables the constitutive relations to model the tension–compression asymmetry besides relative simplicity compared to the other models (Auricchio et al., 1997; Qidwai and Lagoudas, 2000b). The function $\tilde{\Phi}(\boldsymbol{\sigma})$ for this model is given by

$$\tilde{\Phi}(\boldsymbol{\sigma}) = \eta\sqrt{3J_2} + \omega I_1 = \eta\sqrt{\frac{3}{2}\boldsymbol{\sigma}' : \boldsymbol{\sigma}'} + \omega\text{tr}(\boldsymbol{\sigma}), \tag{9}$$

where η and ω are material constants related to the maximum transformation strains during forward phase transformation in tension and compression. The transformation tensor associated with the chosen function is given by $\boldsymbol{\Gamma} = \frac{3\eta}{2}\frac{\boldsymbol{\sigma}'}{\sqrt{3J_2}} + \omega\mathbf{I}$ (Auricchio et al., 1997). The evolution function in this case is similar to the J_2 model by replacing the transformation tensor with the previously derived tensor. It is worth noting that by setting $\omega = 0$ in the J_2-I_1 model, the J_2 model is not recovered because the material constants are calibrated separately for these two models. The material constants in (9) can be calibrated for modeling the volumetric strain or the tension–compression asymmetry. We will use the later method because we are studying the effect of asymmetry of tension–compression response on the bending response of SMAs. However, it is shown that by calibrating the material constants in this manner the model will predict a positive volumetric transformation strain, which is unrealistic[1] (Qidwai and Lagoudas, 2000b). However, we are interested in the bending problem by considering the normal components of stress and strain. The volumetric transformation strain has no effect on our solution. In the special case that the only non-zero stress component is the normal stress σ_x, the transformation tensor is given by

$$\boldsymbol{\Gamma} = \eta\text{sgn}(\sigma_x)\begin{bmatrix} 1 & 0 & 0 \\ 0 & -0.5 & 0 \\ 0 & 0 & -0.5 \end{bmatrix} + \omega\begin{bmatrix} 1 & 0 & 0 \\ 0 & 1 & 0 \\ 0 & 0 & 1 \end{bmatrix}. \tag{10}$$

2.3. Stress–strain relationship for SMAs in pure bending

In the one-dimensional case corresponding to pure bending, substituting the transformation functions (7) and (9) into the expression of thermodynamic force (4) and the transformation criteria (6) enables us to find an explicit expression for the martensitic volume fraction. Using the following relation between the constitutive model parameters

$$\rho\Delta u_0 + \mu_1 = \frac{1}{2}\rho\Delta s_0(M_s + A_f), \quad \rho b^A = -\rho\Delta s_0(A_f - A_s),$$

$$\rho b^M = -\rho\Delta s_0(M_s - M_f), \quad Y = -\frac{1}{2}\rho\Delta s_0(A_f - M_s) - \mu_2,$$

$$\mu_2 = \frac{1}{4}(\rho b^A - \rho b^M), \quad \Delta\alpha = \Delta c = 0, \tag{11}$$

the explicit expressions for the martensitic volume fraction in direct and inverse phase transformation for J_2 and J_2-I_1 models in pure bending after some mathematical manipulation are simplified to read

$$\xi^\pm = \frac{1}{\rho b^\pm}\left\{\aleph|\sigma_x| + \frac{1}{2}\sigma_x^2\Delta S_{11} + \rho\Delta s_0(T - T^\pm)\right\}, \tag{12}$$

for the J_2-based model and

$$\xi^\pm = \frac{1}{\rho b^\pm}\left\{\eta|\sigma_x| + \omega\sigma_x + \frac{1}{2}\sigma_x^2\Delta S_{11} + \rho\Delta s_0(T - T^\pm)\right\}, \tag{13}$$

for the J_2-I_1-based model, where the + and − symbols are used for indicating the loading and unloading, respectively, and $T^+ = M_s$, $T^- = A_f$, $\rho b^+ = \rho b^M$, and $\rho b^- = \rho b^A$. Throughout this paper we use the superscripts + and − for any variable for indicating the forward and reverse phase transformations, respectively.

Substituting the transformation tensors (8) and (10) into the evolution equation, the explicit expressions $\epsilon_x^t = \aleph\text{sgn}(\sigma_x)\xi$ and $\epsilon_x^t = [\eta\text{sgn}(\sigma_x) + \omega]\xi$ are obtained for the J_2 and J_2-I_1 models, respectively. Considering an SMA beam subjected to bending both the axial stress and transformation strain components are positive in the region that is in tension and negative in the region that is subjected to compression. For the sake of simplicity, we write the transformation strain based on J_2 and J_2-I_1 models with the same equation $\epsilon_x^t = (\ell_c\hat{\eta} + \hat{\omega})\xi$, where the loading coefficient ℓ_c is +1 in tension and −1 in compression and the parameters $(\hat{\eta}, \hat{\omega})$ are replaced with (η, ω) for the J_2-I_1 model and replaced with $(\aleph, 0)$ for the J_2 based model. Substituting the resulting transformation strain into (3) gives the following one-dimensional constitutive equation

$$\epsilon_x = (S_{11}^A + \xi\Delta S_{11})\sigma_x + \alpha_A(T - T_0) + (\ell_c\hat{\eta} + \hat{\omega})\xi, \tag{14}$$

where $S_{11}^A = 1/E^A$, $\Delta S_{11} = 1/E^M - 1/E^A$ (E^A and E^M are the elastic muduli of austenite and martensite, respectively). Substituting the martensitic volume fractions (12) and (13), and using the Euler beam theory for the strain-curvature relation $\epsilon_x = -\kappa y$, where κ is the curvature and y is the distance from the neutral axis into (14), the stress–strain relation can be implicitly written as the following cubic equation

$$\sigma_x^3 + a\sigma_x^2 + b\sigma_x + \tilde{c} + \tilde{\kappa}y = 0, \tag{15}$$

where $a, b, \tilde{c}$, and $\tilde{\kappa}$ are constants given by

$$a = \frac{3(\ell_c\hat{\eta} + \hat{\omega})}{\Delta S_{11}}, \quad \tilde{\kappa} = \frac{2\kappa\rho b^\pm}{\Delta S_{11}^2}$$

$$b = \frac{2\rho\Delta s_0(T - T^\pm)}{\Delta S_{11}} + \frac{2(\ell_c\hat{\eta} + \hat{\omega})^2 + 2\rho b^\pm S_{11}^A}{\Delta S_{11}^2}, \tag{16}$$

$$\tilde{c} = \frac{2(\ell_c\hat{\eta} + \hat{\omega})\rho\Delta s_0(T - T^\pm) + 2\rho b^\pm\alpha_A(T - T_0)}{\Delta S_{11}^2}.$$

The cubic Eq. (15) is solved for σ_x as a function of temperature and strain. The acceptable roots[2] for the SMA material in tension and compression are

$$\sigma_t = \frac{1}{6}(A - 108\tilde{\kappa}y + \mathcal{P})^{1/3} - \frac{2b - 2a^2/3}{(A - 108\tilde{\kappa}y + \mathcal{P})^{1/3}} - \frac{a}{3}, \tag{17}$$

$$\sigma_c = \frac{-1}{12}(A - 108\tilde{\kappa}y + \mathcal{P})^{1/3} + \frac{b - a^2/3}{(A - 108\tilde{\kappa}y + \mathcal{P})^{1/3}} - \frac{a}{3}$$
$$- \frac{\sqrt{3}}{2}i\left[\frac{1}{6}(A - 108\tilde{\kappa}y + \mathcal{P})^{1/3} + \frac{2b - 2a^2/3}{(A - 108\tilde{\kappa}y + \mathcal{P})^{1/3}}\right], \tag{18}$$

where $A = 36ab - 108\tilde{c} - 8a^3$, $B = 162\tilde{c} - 54ab + 12a^3$, $C = 12b^3 - 3a^2b^2 - 54ab\tilde{c} + 12a^3\tilde{c} + 81\tilde{c}^2$ and $\mathcal{P} = 12\sqrt{81\tilde{\kappa}^2y^2 + B\tilde{\kappa}y + C}$. It is worth noting that the expressions for stress in tension and compression are real when the SMA material properties are substituted into the coefficients (16). In order to simplify the expressions for stress, we also use the trigonometric form of the roots of the cubic Eq. (15) as (Abramowitz and Stegun, 1964)

---

[1] Experiments on polycrystalline NiTi show a negative change of volume during phase transformation. J_2 models predict a zero transformation volumetric strain and the J_2-I_1 model leads to a positive value. $J_2-J_3-I_1$ models are able to account for a negative transformation strain.

[2] We choose the real positive root for tension, and the real negative root for compression. If there are more than one positive or negative roots, the acceptable root is distinguished by considering the phase transformation start and finish stresses (30).

$$\sigma_t = \cos\left(\frac{1}{3}\tan^{-1}\theta\right)\mathcal{G} - a/3, \tag{19}$$

$$\sigma_c = \frac{1}{2}\cos\left(\frac{1}{3}\tan^{-1}\theta - \frac{2\pi}{3}\right)\mathcal{G} + \frac{\sqrt{3}}{2}\sin\left(\frac{1}{3}\tan^{-1}\theta - \frac{2\pi}{3}\right)\mathcal{G} - a/3, \tag{20}$$

where $\theta = 12\sqrt{-81\tilde{\kappa}^2 y^2 - B\tilde{\kappa}y - C}/(A - 108\,\tilde{\kappa}y)$, and $\mathcal{G} = \frac{1}{3}(A^2 - 144C)^{1/6}$. The explicit expressions in (19) give the exact value of stress. However, we need a simplified expression to calculate an explicit expression for bending moment later. As it will be shown in Section 4, the typical values of material properties for SMAs lead to a large value for θ in (19). Using the trigonometric identity $\tan^{-1}\theta = \pi/2 - \tan^{-1}(1/\theta)$, the argument of tangent inverse is small and can be approximated as $\tan^{-1}\theta \simeq \pi/2 - 1/\theta$. Substituting this approximation in (19) and using the fact that the parameter $\beta = 1/(3\theta)$ is also small, and considering the approximations $\cos\beta \simeq 1 - \beta^2/2$, and $\sin\beta \simeq \beta$, the stresses in tension and compression are given by

$$\sigma_t = \left[\left(1 - \frac{1}{2}\beta^2\right)\cos\varphi + \beta\sin\varphi\right]\mathcal{G} - \frac{a}{3}, \tag{21}$$

$$\sigma_c = \left[\left(1 - \frac{1}{2}\beta^2\right)\cos\varphi + \beta\sin\varphi\right]\mathcal{G} + \frac{\sqrt{3}}{2}\left[\beta\cos\varphi - \left(1 - \frac{1}{2}\beta^2\right)\sin\varphi\right]\mathcal{G} - \frac{a}{3}, \tag{22}$$

where $\varphi = \pi/6$. After some algebraic simplifications, the stress–strain relationship in tension and compression can be unified using the load condition coefficient ℓ_c as

$$\sigma = \left[\ell_c\left(1 - \frac{1}{2}\beta^2\right)\cos\varphi + \beta\sin\varphi\right]\mathcal{G} - \frac{a}{3}. \tag{23}$$

We will present a detailed numerical study of the accuracy of the above approximation for obtaining (21) from the exact expressions in (19) for different curvature values in Section 4. It will be shown that these approximate formulas give accurate results even for large curvatures.

3. Bending moment–curvature relationship for SMAs in bending

In this section we present a closed-form relationship between the bending moment and curvature in SMAs subjected to bending using the explicit stress–strain relations obtained in the previous section. We will introduce the formulas with some different simplifying assumptions. The accuracy of each approximation is numerically studied in Section 4 versus the exact solution obtained by using the exact stress–strain relationships (19) or (17) and using numerical integration in the cross section for obtaining the bending moment–curvature response.

The bending moment–curvature relationship for an SMA beam with an arbitrary cross section is given by $M = \int_\Omega y\sigma(y)dA$, where M is the bending moment, y is the distance from the neutral axis, and Ω is the cross section. In the most general case, the cross section is divided into three regions: an elastic core in which the phase transformation has not started, a middle part with phase transformation, and the outer part in which the material is fully transformed to martensite. In order to calculate the total bending moment, the bending moment in each part should be found and summed in the whole cross section. The most complicated section to be solved is the middle part with active phase transformation. However, the bending moment in this section can be calculated explicitly by using the stress distributions given in (23). In addition to the bending moment obtained using the complete stress

expression (23), we present two more explicit expressions for the bending moment obtained by imposing simplifications on the stress distribution. We will numerically study the accuracy of these simplifying assumptions in Section 4. The simplified relations can be later used for developing closed-form solutions in more complicated cases, e.g. for studying the large deflection of SMA cantilevers. We start with the complete stress distribution in (23). For calculating the bending moment, the stress distribution (23) should be used only in the portion of the cross section with phase transformation. We present a method for finding the boundaries of this section (see (32)). For a rectangular cross section, we can write

$$\mathcal{I}^1 = \int y\sigma(y)wdy$$

$$= \frac{-w\mathcal{G}\sqrt{R}(-54\tilde{\kappa}y + A + B)\sin\varphi}{2916\tilde{\kappa}^2} - \frac{w\ell_c\mathcal{G}y(3A + 2B)\cos\varphi}{2916\tilde{\kappa}}$$

$$+ \frac{19}{36}wy^2\ell_c\mathcal{G}\cos\varphi - \frac{1}{6}wy^2 a - \frac{w\mathcal{G}\tan^{-1}(S)(B^2 - 108C + AB)\sin\varphi}{2^3 3^8 \tilde{\kappa}^2}$$

$$+ \frac{w\ell_c\mathcal{G}\ln(-R)(-1296C + 9A^2 + 24AB + 16B^2)\cos\varphi}{2^6 3^{10}\tilde{\kappa}^2}$$

$$+ w\ell_c\mathcal{G}\tanh^{-1}(Q)\cos\varphi\left(\frac{-3888C(A + B) + 9A^2 B + 24AB^2 + 16B^3}{2^5 3^{10}\tilde{\kappa}\sqrt{B^2\tilde{\kappa}^2 - 324\tilde{\kappa}^2 C}}\right) + \mathbb{C}_1, \tag{24}$$

where w is the cross section width, $\mathbb{C}_1$ is a constant of integration, and

$$R = -81\tilde{k}^2 y^2 - Bky - C, \quad Q = \frac{162\tilde{k}^2 y + B\tilde{k}}{\sqrt{B^2\tilde{k}^2 - 324\tilde{k}^2 C}},$$

$$S = \frac{9\tilde{k}}{\sqrt{R}}\left(y + \frac{1}{162}\frac{B}{\tilde{k}}\right). \tag{25}$$

The other parameters in (24) are all defined in the previous sections. We use this expression for calculating the total bending moment in the cross section later on. Before doing that, we first present two more expressions for this integral using the following simplifications. Considering the typical material properties for polycrystalline SMAs, it can be shown that in the term $\theta = 12\sqrt{-81\tilde{\kappa}^2 y^2 - B\tilde{\kappa}y - C}/(A - 108\,\tilde{\kappa}y)$, $|-C| \gg |-B\tilde{\kappa}y| > |-81\tilde{\kappa}^2 y^2|$. We consider two simplifying approximations in calculating the bending moment by ignoring the first term and the first two terms in the nominator of the expression for θ. The accuracy of these approximations will be numerically studied in Section 4.1. By ignoring the first term $(-81\tilde{\kappa}^2 y^2)$, the integral required for calculating the bending moment for a rectangular cross section is given by

$$\mathcal{I}^2 = \int y\sigma(y)wdy$$

$$= \frac{6w\mathcal{G}(-B\tilde{\kappa}y - C)^{5/2}\sin\varphi}{5B^3\tilde{\kappa}^2} + \frac{4w\mathcal{G}C(-B\tilde{\kappa}y - C)^{3/2}\sin\varphi}{B^3\tilde{\kappa}^2}$$

$$+ \frac{w\mathcal{G}A(-B\tilde{\kappa}y - C)^{3/2}\sin\varphi}{54B^2\tilde{\kappa}^2} + \frac{w\mathcal{G}CA\sqrt{-B\tilde{\kappa}y - C}\sin\varphi}{18B^2\tilde{\kappa}^2}$$

$$+ \frac{6w\mathcal{G}C^2\sqrt{-B\tilde{\kappa}y - C}\sin\varphi}{B^3\tilde{\kappa}^2} + \frac{3w\ell_c\mathcal{G}y^3\cos\varphi}{2B}$$

$$+ \frac{1}{2}wy^2\ell_c\mathcal{G}\cos\varphi - \frac{wy^2\ell_c\mathcal{G}A\cos\varphi}{24B} - \frac{1}{6}wy^2 a$$

$$- \frac{9wy^2\ell_c\mathcal{G}C\cos\varphi}{4B^2} + \frac{w\ell_c\mathcal{G}yA^2\cos\varphi}{2592B\tilde{\kappa}} + \frac{w\ell_c\mathcal{G}yCA\cos\varphi}{12B^2\tilde{\kappa}}$$

$$- \frac{w\ell_c\mathcal{G}CA^2\ln(B\tilde{\kappa}y + C)\cos\varphi}{2592B^2\tilde{\kappa}^2} + \frac{9w\ell_c\mathcal{G}yC^2\cos\varphi}{2B^3\tilde{\kappa}}$$

$$- \frac{w\ell_c\mathcal{G}C^2 A\ln(B\tilde{\kappa}y + C)\cos\varphi}{12B^3\tilde{\kappa}^2}$$

$$- \frac{9w\ell_c\mathcal{G}C^3\ln(B\tilde{\kappa}y + C)\cos\varphi}{2B^4\tilde{\kappa}^2} + \mathbb{C}_2, \tag{26}$$

where $\mathbb{C}_2$ is a constant of integration. By ignoring the first two terms, this integral is simplified to read

$$
\begin{aligned}
\mathcal{I}^3 = \int y\sigma(y)w\,dy &= \frac{9}{8}\frac{w\ell_c\mathcal{G}\tilde{k}^2 y^4 \cos\varphi}{C} \\
&+ \frac{1}{3}\left(\frac{-1}{12}\frac{w\ell_c A\tilde{k}\cos\varphi}{C} - 3\frac{w\tilde{k}\sin\varphi}{\sqrt{-C}}\right)\mathcal{G}y^3 \\
&+ \frac{w}{2}\left\{\left[\ell_c\cos\varphi\left(1+\frac{1}{2592}\frac{A^2}{C}\right) + \frac{1}{36}\frac{A\sin\varphi}{\sqrt{-C}}\right]\mathcal{G} - \frac{1}{3}a\right\}y^2 + \mathbb{C}_3,
\end{aligned}
$$
(27)

where $\mathbb{C}_3$ is a constant of integration. The integrals (24)–(27) are calculated for a rectangular cross section. We study the circular cross section later in this section. For obtaining a complete description of the moment–curvature relation, it is necessary to find the boundaries of the region in which the phase transformation occurs. We obtain these boundaries for the loading phase first. Later we show that a different approach should be used for unloading. In the most general case in loading, the cross section is divided into three sections. A schematic of the cross section for a rectangular superelastic beam is shown in Fig. 1. The first region includes the neutral axis and the phase transformation has not started in this region ($\xi = 0$). In the second region (region II) the phase transformation has started but has not been completed ($0 < \xi < 1$). The third region (region III) contains the material with completed phase transformation from austenite to martensite ($\xi = 1$).

When using the J_2-based model, the neutral axis is located at the centroid of the beam ($Y_{NA} = 0$ in Fig. 1) and the three regions are symmetric with respect to the center line. However, for the J_2-I_1-based model, the neutral axis is not located on the center line. To find the neutral axis location in this case, the force equilibrium in each cross section along the beam axis ($\sum F = 0$) should be enforced, which reads

$$
\begin{aligned}
&\frac{1}{2}E^A\kappa y_{1t}^2 + \left(\tilde{\mathcal{I}}|_{y=y_{1t}} - \tilde{\mathcal{I}}|_{y=y_{2t}}\right) + E^M\left[\frac{1}{2}\kappa\left(y_{2t}^2 - \frac{h_t^2}{4}\right) - H^t\left(y_{2t} + \frac{h_t}{2}\right)\right] \\
&- \frac{1}{2}E^A\kappa y_{1c}^2 + \left(\tilde{\mathcal{I}}|_{y=y_{2c}} - \tilde{\mathcal{I}}|_{y=y_{1c}}\right) + E^M\left[\frac{1}{2}\kappa\left(\frac{h_c^2}{4} - y_{2c}^2\right) - H^c\left(\frac{h_c}{2} - y_{2c}\right)\right] = 0,
\end{aligned}
$$
(28)

where H^t and H^c are the maximum transformation strains in tension and compression, respectively. The parameters h_t and h_c are the maximum distance from the neutral axis in the tension and compression regions, respectively (see Fig. 1). The first three terms in (28) correspond to the force in sections below the neutral axis subjected to tension, and the next terms represent the force above the neutral axis in compression (a positive curvature is assumed). The terms containing $\tilde{\mathcal{I}}$ represent the force corresponding to region II with $0 < \xi < 1$ given by

$$
\begin{aligned}
\tilde{\mathcal{I}} &= \int \sigma(y)\,dy \\
&= \ell_c\mathcal{G}y\cos\varphi - \frac{\ell_c\mathcal{G}y\left(-27B\tilde{k}y + BA + 54C\right)\cos\varphi}{12B^2} - \frac{1}{3}ay \\
&- \frac{2\mathcal{G}\left(-B\tilde{k}y - C\right)^{3/2}\sin\varphi}{B^2\tilde{k}} \\
&- \frac{\mathcal{G}\sqrt{-B\tilde{k}y - C}(BA + 108C)\sin\varphi}{18B^2\tilde{k}} \\
&+ \frac{\ell_c\mathcal{G}\ln\left(B\tilde{k}y + C\right)\left(A^2B^2 + 216CAB + 11664C^2\right)\cos\varphi}{2592B^3\tilde{k}} + \mathbb{C}_4,
\end{aligned}
$$
(29)

where $\mathbb{C}_4$ is a constant of integration. In (28) we need to calculate the values of y_{1t}, y_{2t}, y_{1c}, and y_{2c} to obtain the neutral axis position. The stress values corresponding to the start and finish of phase transformation during loading phase can be calculated by replacing $\xi^+ = 0$ and $\xi^+ = 1$ into (13) and solving for stress. These are given by

$$
\sigma_s = \frac{\sqrt{(\ell_c\hat{\eta} + \hat{\omega})^2 - 2\Delta S_{11}\rho\Delta s_0(T - M_s)} - (\ell_c\hat{\eta} + \hat{\omega})}{\Delta S_{11}},
$$
(30)

$$
\sigma_f = \frac{\sqrt{(\ell_c\hat{\eta} + \hat{\omega})^2 - 2\Delta S_{11}\left(\rho\Delta s_0(T - M_s) - \rho b^M\right)} - (\ell_c\hat{\eta} + \hat{\omega})}{\Delta S_{11}},
$$
(31)

where the loading factor ℓ_c is equal to $+1$ in tension and -1 in compression. Using these stress values the boundaries of various regions in the cross section are given by

$$
\begin{aligned}
y_{1t} &= \frac{\sigma_s|_{\ell_c=1}}{\kappa E^A}, \quad y_{2t} = \frac{(\hat{\eta} + \hat{\omega})E^M + \sigma_f|_{\ell_c=1}}{\kappa E^M}, \\
y_{1c} &= \frac{\sigma_s|_{\ell_c=-1}}{\kappa E^A}, \quad y_{2c} = \frac{(-\hat{\eta} + \hat{\omega})E^M + \sigma_f|_{\ell_c=-1}}{\kappa E^M}.
\end{aligned}
$$
(32)

Substituting (29)–(32) into (28) and considering the fact that $h_c = h - h_t$, where h is the cross section height, this equation can be solved for h_t. This gives the neutral axis position corresponding to κ. It is worth noting that this formulation corresponds to the most general case in which the cross section is divided into three regions. It is obvious that if $|y_{2t}| > h_t$ or $y_{2c} > h_c$, region III is not formed in the tension or compression part of the cross section and the above equations can be modified by eliminating the terms associated with this region.

Bending moment at each cross section along the length of the superelastic beam is related to the curvature by

$$
\begin{aligned}
M &= -\frac{1}{3}E^A\kappa w(y_{1c}^3 - y_{1t}^3) + \left(\mathcal{I}^i|_{y=y_{2c}} - \mathcal{I}^i|_{y=y_{1c}}\right) \\
&+ E^M w\left[\frac{1}{3}\kappa\left(\frac{h_c^3}{8} - y_{2c}^3\right) - H^c\left(\frac{h_c^2}{4} - y_{2c}^2\right)\right] \\
&+ \left(\mathcal{I}^i|_{y=y_{1t}} - \mathcal{I}^i|_{y=y_{2t}}\right) \\
&+ E^M w\left[\frac{1}{3}\kappa\left(y_{2t}^3 - \frac{h_t^3}{8}\right) - H^c\left(y_{2t}^2 - \frac{h_t^2}{4}\right)\right],
\end{aligned}
$$
(33)

where the superscript i is replaced by 1, 2, or 3 for different approximations given in (24)–(27). It is worth noting that when the terms $\mathcal{I}$ are evaluated in tension regions, the loading coefficient $\ell_c = 1$ and in the compression regions $\ell_c = -1$. The solution procedure for the loading phase is as follows. Bending moment along the beam axis is calculated by considering the external force and the boundary conditions. At each cross section bending moment is known and the curvature should be found by solving the nonlinear algebraic Eq. (33). In the case of the J_2-based model, this equation can be solved independently because the neutral axis location is known due to symmetry, i.e. $h_c = h_t = h/2$. However, in the case of using the J_2-I_1-based model, the neutral axis position is unknown and should be obtained by solving (28) in which the curvature is assumed known. For solving these equations simultaneously, a numerical scheme is used (Forsythe et al., 1976). In this numerical method, in each iteration, curvature κ in (33) is given an initial value. This initial value is substituted into (28) and the neutral axis position is obtained. The calculated neutral axis position is returned to evaluate the right-hand side of (33). Comparing the calculated bending moment at that cross section with the bending moment obtained from the external force, curvature is modified (Forsythe et al., 1976). The iterations are stopped when a tolerance is achieved

between the applied bending moment at each cross section and the right-hand side of (33). When the curvature is found the lateral deflection is calculated using $\kappa = \frac{d^2 v}{dx^2}$, where v is the lateral deflection and x is measured along the beam axis. The integration constants in curvature-lateral deflection relationship are found by imposing the appropriate boundary conditions.

In the unloading phase, in the most general case the cross section may be divided into three regions. The material in the inner region with elastic response in loading ($y_{1t} < y < y_{1c}$) experiences elastic unloading. The outer regions with phase transformation in loading are divided into two regions during unloading; one with elastic unloading and the other one with reverse phase transformation in unloading. To obtain the boundaries of these regions consider a generic point in the cross section. If we denote the martensitic volume fraction at the end of loading for this point by ξ^*, the critical stress for the start of reverse phase transformation in unloading is given by replacing ξ^- in (12) or (13) by ξ^* and solving the resulting equation for stress. Using the properties defined for the evolution equation (see below (13) for definitions), this critical stress is given by

$$\sigma_c = \frac{\ell_c \sqrt{(\ell_c \hat{\eta} + \hat{\omega})^2 - 2\Delta S_{11} \rho \Delta s_0 (T - A_f) - \rho b^A \xi^*}}{\Delta S_{11}}. \tag{34}$$

During unloading, the elastic change of stress at a generic location is calculated by $\Delta \sigma = -(E^A + \xi^* \Delta E)(-\kappa^* y + \kappa_u y)$, where y is the distance of the point from the neutral axis. The parameters κ^* and κ_u are the curvature of the corresponding cross section at the end of the loading phase and the curvature in unloading, respectively. Now we can evaluate the start of reverse phase transformation by comparing the stress $\sigma_e = \sigma^* - \Delta \sigma$ (σ^* is the stress value at the end of loading phase) with σ_c. For $|\sigma_e| > |\sigma_c|$, the phase transformation in unloading has not started. In this case stress is equal to σ_e and $\xi = \xi^*$. If $|\sigma_e| \leqslant |\sigma_c|$, the reverse phase transformation has started. The stress and martensitic volume fraction are obtained from (12), (13), and (23) by considering the superscript "-" and the appropriate loading condition parameter $\ell_c = \pm 1$. For the sake of brevity, the details of the bending moment–curvature relations and the process of finding the neutral axis position in unloading are not presented here. However, this procedure is very similar to that of the loading case.

For analyzing beams with circular cross sections a similar method is used where Ω is the area enclosed by the horizontal chords at y_{1t} and y_{2t}, and also the area between y_{1c} and y_{2c} in the cross section. In this case, we use a trapezoidal numerical integration method to obtain the bending moment–curvature relationship.

4. Numerical results

In this section, several case studies are presented for superelastic beams with circular and rectangular cross sections subjected to loading–unloading cycles. The results of both J_2 and J_2–I_1 models are presented. The J_2-based solution is compared with a three-dimensional finite element model and the J_2–I_1 results are presented to show the effect of taking into account the tension–compression asymmetry on the bending response of superelastic beams. Some experimental data for bending of a nickel–titanium micropillar are used to verify the applicability of the present method for modeling bending in the micro scale. The available material response in compression and bending are used for extracting the material response in tension, which is very difficult to measure in experiments. The resulting tensile and compressive properties are compared with the nickel–titanium constitutive relations and it is shown that the predicted response in tension is in good agreement with the single-crystal theoretical response (see the end of Section 4.6).

4.1. The accuracy of the proposed approximations

In Section 2.3 we presented the exact stress distribution (19). Using this stress distribution needs a numerical integration for obtaining the bending moment–curvature relation. Using some assumptions an approximate stress distribution is given in (23), which can be used for calculating explicit expressions for the the bending moment–curvature relation. We used three different simplifying assumptions for calculating the bending moment as a function of curvature (see $\mathcal{I}^i$, $i = 1, 2, 3$ in (24)–(27)). In this section we compare the bending moment–curvature relationship obtained by the exact stress distribution and numerical trapezoidal integration with the results of the three approximations. A rectangular cross section with $h = 1$ cm and width $w = 1.5$ mm is considered. The J_2-based model is used for this comparison. The material properties for Ni$_{50}$Ti$_{50}$ (Jacobus et al., 1996) are used for obtaining the necessary constants in the constitutive relations (see Qidwai and Lagoudas (2000b) for details of extracting constitutive model constants from experimental data): $E^A = 72$ MPa, $E^M = 30$ MPa, $v^A = v^M = 0.42$, $\rho c^A = \rho c^M = 2.6 \times 10^6$ J/(m^3 K), $H^t = 0.05$, $H^c = -0.035$, $(d\sigma/dT)^A_t = 8.4 \times 10^6$ J/(m^3 K), $\rho \Delta s_0 = -H^t (d\sigma/dT)^A_t = -0.42 \times 10^6$ J/(m^3 K), $A_f = 281.6$ K, $A_s = 272.7$ K, $M_f = 238.8$ K, $M_s = 254.9$ K. For implementing the J_2-based model, the constants in the transformation function are set to $\hat{\eta} = \aleph = H^t$, and $\hat{\omega} = 0$. The temperature is $T = T_0 = 300$ K and an isothermal loading–unloading process is assumed (see Mirzaeifar et al. (2011a) for a detailed study of isothermal process and thermo-mechanical coupling in the response of SMAs). The bending moment–curvature relation is depicted in Fig. 2. As it is seen, all the approximations are in good agreement with the solution obtained form the exact stress distribution even for large curvature values. We use the approximation II (given in (26)) throughout this paper. We use the third approximation in a future communication for considering the large deflection effects.

4.2. J_2-based model

In this section the results of the J_2-based model are presented. We compare the analytical results obtained from the present formulation with those of a three-dimensional finite element simulation. The three-dimensional constitutive relations of Section 2 are used and an appropriate user subroutine (UMAT) is written by FORTRAN in the commercially available finite element program ABAQUS that enables this code to model SMA structures using solid elements and some two-dimensional elements. The details of implementing the constitutive equations in a displacement-based finite element formulation are given in Mirzaeifar et al. (2009). The finite element framework is validated by comparing its results with many experimental tests and analytical solutions in Mirzaeifar et al. (2010, 2011c,b). An SMA cantilever with length $L = 10$ cm is considered in this section. The rectangular cross section has a height of $h = 1$ cm and width $w = 1.5$ mm. Three-dimensional quadratic brick elements with reduced integration (element C3D20R in ABAQUS) are used in the finite element method. A convergence analysis is performed for choosing the appropriate number of elements by considering the normal stress distribution in the cross section and the load–displacement response as the convergence criteria. The stress distribution is considered to be converged when the maximum difference is smaller than 0.1 MPa and the convergence criterion of the maximum difference for the load–displacement response is 10 N. A total of 6000 elements are used for modeling the cantilever beam ($100 \times 20 \times 3$ elements in length, width, and thickness directions). All the finite element simulations are done using this mesh. The material properties are the same as those of the case study in Section 4.1. The temperature is $T = T_0 = 300$ K and an isothermal loading–unloading process is
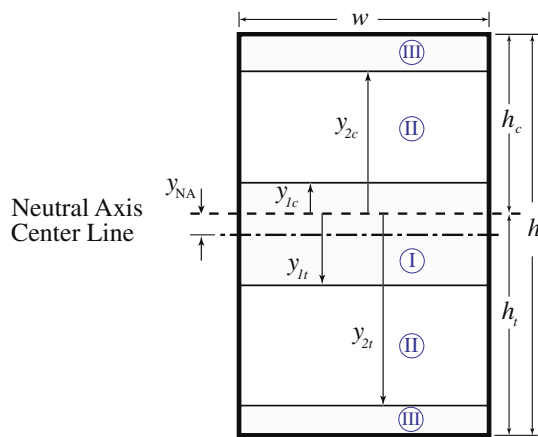
Fig. 1. A schematic of the rectangular cross section.

assumed. The superelastic cantilever is subjected to a transverse tip load. The load-tip deflection is calculated by the present analytical method and the results are compared with the numerical simulation results in Fig. 3.

As it is shown, even for this relatively large deflection (the tip deflection is four times the height of the beam), the results are in good agreement (with a maximum of 14% error). The finite element results show stiffening at the end of loading phase as the slope of force–deflection increases while the analytical solution predicts an almost constant gradient. This difference is mainly caused by the nonlinear geometric effects that are ignored in the present solution and included in the numerical simulations. It is worth noting that the finite element simulation is completed in about two hours on a 2 GHz CPU with 2 GB RAM while the analytic solutions are obtained in a few seconds on the same system. Also as it is seen in Fig. 3, the numerical simulation in unloading is not completed. This happens due to some convergence issues in most numerical simulations during unloading, especially in the case of large deflections or complicated geometries. While achieving convergence in the finite element simulation requires an excessive effort by refining the mesh size and modifying the numerical algorithms, the present analytic solution is a reliable method. The present method can also be used as a benchmark for validating the numerical simulations. In order to study the
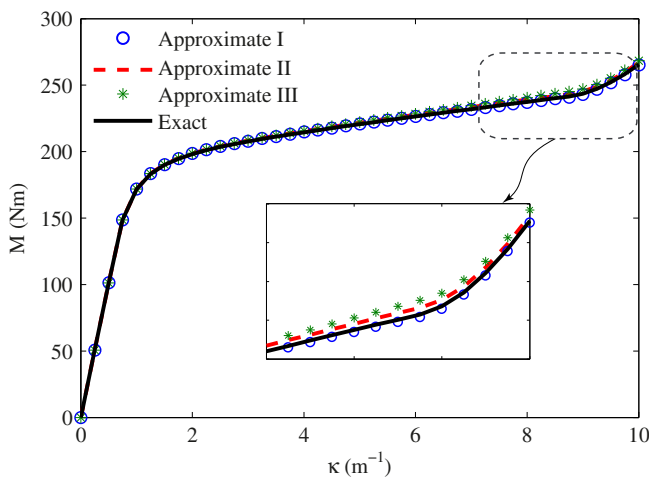
capability of the present formulation in calculating the stress and martensitic volume fraction distributions, the cross section of the superelastic cantilever at the clamped edge is considered. The stress distribution at the end of the loading phase is shown in Fig. 4(a) and the martensitic volume fraction is shown in Fig. 4(b). As it is shown the closed-form solution calculates both the stress and martensitic volume fractions accurately. It is worth noting that in the finite element simulation the outputs are averaged between integration points and this makes the results smooth compared to the analytical solution. As it is seen in these figures, the core remains austenite without phase transformation. By considering pure bending, the stress around the neutral axis is zero and there is always an austenite core without phase transformation even for large deflections. By considering the shear effect in bending, the stress at the core is nonzero which may cause phase transformation at the core as well. However, except for very thick beams the pure bending theory gives accurate results and this is reflected in comparison of the results with the finite element solution that considers the shear effect.

The contour plots of the stress and martensitic volume fraction distributions at the end of the loading phase obtained from the present closed-form solution are depicted in Fig. 5 and compared with the finite element results. As it is shown, the deformed shape obtained by the present method is slightly different from the numerical simulation prediction. Also, the analytic solution (in this section we are using the J_2-based model) is predicting symmetric stress and martensitic volume fraction distributions, while the finite element results show a slight asymmetry along the beam axis. Note that in our solution the nonlinear geometry effects and the displacement along the beam axis direction are ignored while the numerical simulations show a minor deflection along the axis due to geometric nonlinearities. As shown in Figs. 3–5, the present method gives accurate results even for the large deflection chosen in these case studies. It is worth nothing that the accuracy of the results based on small deflection assumption is geometry dependent. The geometry in the above case studies is chosen such that phase transformation starts in the cross section even for moderate tip deflections (in the order of thickness). If other geometries are chosen (e.g. the same beam in another direction with height $h = 1.5$ mm and width $w = 1$ cm), very large deflections are required for the phase transformation to start, and using the solutions based on the small deflection assumption leads to large errors in those cases. However, there are numerous applications for which the approach of this paper gives accurate results (e.g. the micropillar studied at the end of this section).

As another case study, consider a superelastic cantilever with circular cross section. The material properties are the same as those of the previous case study and the dimensions are $R = 5$ mm and $L = 10$ cm, where R is the cross section radius. A total of 9600 three-dimensional quadratic brick elements with reduced integration (element C3D20R in ABAQUS) are used in the finite element model (a cross section of the mesh is shown in Fig. 8). The cantilever is clamped at one end and a transverse load is applied at the other end as shown in Fig. 6. The applied force versus the tip deflection obtained by the present analytical method is shown in Fig. 6 and compared with the finite element results. As it is seen, the finite element results again suffer from convergence issues during the unloading phase and this causes the solution to terminate before completion. The results are in good agreement (with a maximum of 11% error) even for the relatively large deflection (four times the bar diameter).

The results for the calculated stress and martensitic volume fraction corresponding to the end of the loading phase at the clamped edge are compared in Fig. 7. The results are depicted along a vertical path passing through the center of the cross section at the clamped edge.
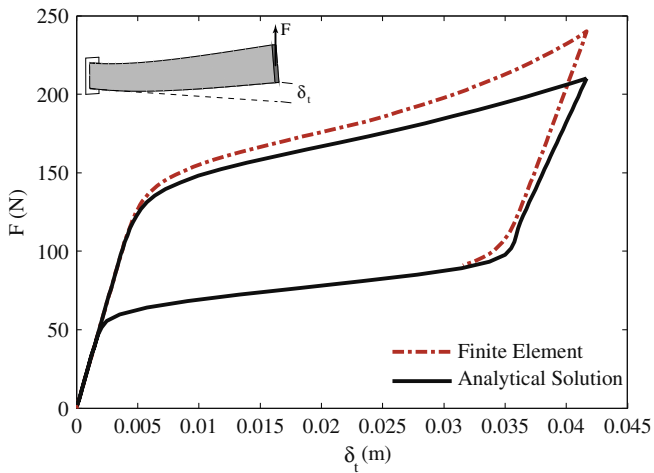

Fig. 2. The bending moment–curvature relationship calculated by the exact stress distribution with trapezoidal integration, and three different approximate explicit integrals (24), (26), and (27) of Section 3.

Fig. 3. Force versus tip deflection for an SMA beam with rectangular cross section (b = 1.5 mm, h = 1 cm, and L = 10 cm).

The contour plots of the stress and martensitic volume fraction distributions are shown in Fig. 8. These contours are plotted for a vertical section passing through the axis of the bar (see Fig. 6 for the geometry). As mentioned earlier, a slight difference in the deformed shape and the asymmetry of distributions observed in the finite element outputs both result from ignoring the geometric nonlinearities in the present formulation. In the results presented in this section, both the numerical simulations and the analytic solutions are based on the J_2 model. The effect of taking into account the tension–compression asymmetry on the response of SMAs is considered by using the J_2–I_1-based model and the results are presented in the next section.

4.3. Effect of tension–compression asymmetry on the bending response of SMAs

Most shape memory alloys including NiTi exhibit significant different responses in tension and compression when subjected to uniaxial loading. Bending is readily affected by this phenomenon because the material is subjected to both tension and compression in bending. We presented a J_2–I_1-based model capable of modeling the tension–compression asymmetry in Sections 2 and 3. The constitutive model parameters should be calibrated using the experimental data. Denoting the maximum transformation strain in tension and compression by H^t and H^c, respectively, the J_2–I_1 model

parameters are given by $\hat{\eta} = \eta = \frac{1}{2}(H^t + |H^c|)$, and $\hat{\omega} = \omega = \frac{1}{2}(H^t - |H^c|)$. We consider the material properties used in the previous section and modify the constitutive parameters by implementing the above modifications. The response of a NiTi alloy with these properties in uniaxial compression is calculated using both the J_2 and J_2–I_1 models as shown in Fig. 9. It is worth noting that the material response in tension is identical for both models and equivalent to the results of the J_2-based model in Fig. 9 with positive stress and strain values. As it is shown in Fig. 9, the J_2–I_1-based model predicts the start of the phase transformation at larger absolute values of stress, and also predicts a lower compressive strain for completion of phase transformation compared to the J_2-based model. This phenomenon is in agreement with experimental data (Gall et al., 1999a,b). The experimental data of Jacobus et al. (1996) were used in Qidwai and Lagoudas (2000b) and the accuracy of the presented J_2–I_1-based model was studied for modeling uniaxial loading. We are using the same constitutive model and material properties for studying bending of SMA beams.

Consider a cantilever superelastic beam with rectangular cross section with the same dimensions, temperature, and boundary conditions as those of the case study of Section 4.2. For comparison purposes we study the results of J_2 and J_2–I_1-based models to analyze the effect of taking into account the tension–compression asymmetry on the bending response of superelastic beams. The tip deflection versus applied force is depicted in Fig. 10. Two different case studies are solved with the J_2 model. In one case the beam is subjected to the same force as in the J_2–I_1-based case study, and in the other one the tip deflections of both beams are equal. As it is shown, the tension–compression asymmetry significantly affects the bending response. In the same deflection case, a maximum of 16% difference is seen in the applied force and in the same force case, the tip deflection differs by a maximum value of 41% at the end of the loading phase. The stress and martensitic volume fraction distributions at the clamped edge are shown in Fig. 11 for this case study at the end of the loading phase. As it is seen in Fig. 11(a), the J_2–I_1 model predicts the zero stress above the cross section center (y = 0). The non-symmetric martensitic volume fraction distribution is shown in Fig. 11(b). It is worth noting that the minor symmetry observed in the FE results is caused by the effect of large deflections, mainly because the load at the tip is considered always vertical in the FE analysis (the load is not rotating as the tip rotates).

The zero stress point determines the neutral axis position that is found by solving (28) as explained in Section 3. As expected (see Fig. 9), the absolute value of stress predicted by the J_2–I_1-based model is larger compared to the predicted values by the J_2-based model. This causes a larger force at the compression portion of
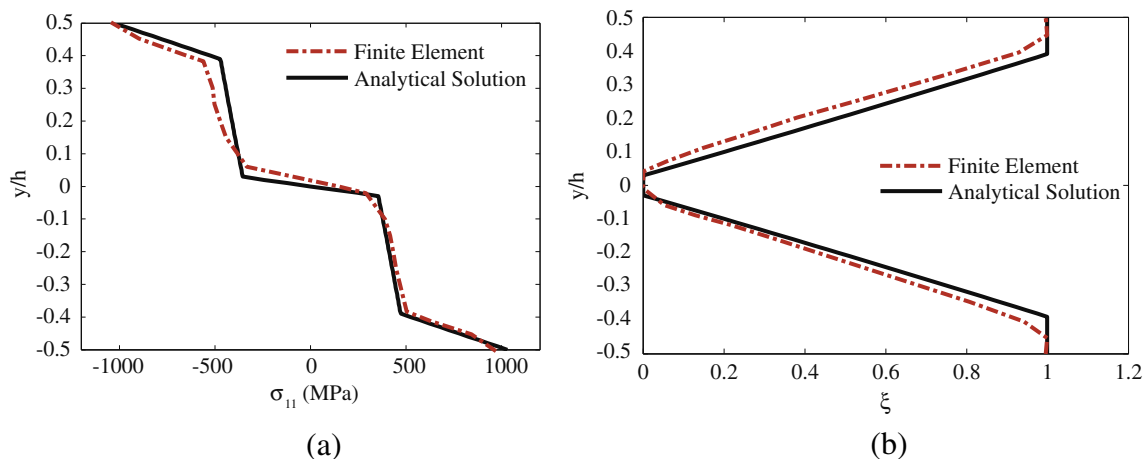

(a)

(b)

Fig. 4. Comparison of the finite element and analytical results for (a) normal stress and (b) martensitic volume fraction distribution at the clamped edge of an SMA beam with rectangular cross section subjected to bending. The results correspond to the end of the loading phase (see Fig. 3).

the cross section, and the neutral axis is shifted up toward the compression part in order to satisfy equilibrium. It is worth noting that the height of the phase transformation area is smaller in the compression part due to smaller maximum compressive transformation strain (see Fig. 9) and this causes a slight downward movement of the neutral axis towards the centerline as the phase transformation area (section II in Fig. 1) is formed in the cross section. To have a detailed view of the neutral axis position with respect to the applied bending moment, this position is plotted along the axis of the beam (in which the bending moment is varying linearly) in Fig. 12. As it is shown, in the regions far from the clamped edge in which the material responds elastically due to small bending moments, the neutral axis coincides with the centerline. Increasing the bending moment (decreasing x on the horizontal axis), the neutral axis distance from the centroid increases up to a specific bending moment value ($M = 17.5$ Nm at $x = 1.75$ cm in the present case study). Increasing the bending moment above this critical value, the neutral axis distance from the centroid decreases slightly due to spread of the fully transformed area.

The contour plots of martensitic volume fraction at the end of the loading phase near the clamped edge are shown in Fig. 13 and the results are compared for the J_2 and J_2-I_1 models (for case study with identical tip deflections). An asymmetric distribution is clearly seen in Fig. 13(a) and the neutral axis position is shown. As it is seen, the neutral axis coincides with the centerline in the regions far from the clamped edge where the phase transformation has not started. Fig. 10 shows the significant effect of this asymmetry on the force–deflection response of the superelastic cantilever.

4.4. Materials with large tension–compression asymmetries

It has been observed in experiments that the material properties in shape memory alloys, particularly NiTi, are strongly affected by the deformation processing. Frick et al. (2004) studied the properties of cast and deformation processed polycrystalline NiTi (Ti-50.9 at. pct Ni) bars. They showed that while the material response for the cast NiTi samples is almost symmetric in tension and compression, a cast, hot rolled, then cold drawn material exhibits a very large asymmetry in tension–compression response. The maximum transformation strain in tension is reported more than two times the maximum transformation strain in compression for the hot rolled, then cold drawn material with a significant difference in the stress levels in the stress–strain plateau (see Fig. 14). Such a large asymmetry in tension–compression response causes numerical instabilities in the finite element simulations. However, our closed-form solution does not suffer from such instabilities. In order to study the applicability of our analytic solution for modeling bending of SMA beams with very large tension–compression asymmetry, a superelastic beam with rectangular cross section is considered. The geometry and boundary conditions are the same as those of the case studies in Section 4.2. The experimental results for the stress–strain response of the material is shown in Fig. 14. The material properties in the constitutive model are calibrated as follows: $E^A = 63$ MPa, $E^M = 35$ MPa, $v^A = v^M = 0.3$, $H^t = 0.047$, $H^c = -0.02$, $(d\sigma/dT)_t^A = 6.4 \times 10^6$ J/(m^3 K), $\rho\Delta s_0 = -H^t(d\sigma/dT)_t^A = -0.3008\times 10^6$ J/(m^3 K), $A_f = 300$ K, $A_s = 273$ K, $M_f = 218$ K, $M_s = 254$ K. We use the J_2-I_1-based model for analyzing this problem by setting $\hat{\eta} = \eta = \frac{1}{2}(H^t + |H^c|)$ and $\hat{\omega} = \omega = \frac{1}{2}(H^t - |H^c|)$. The ambient temperature is $T = T_0 = 27$ °C. The model prediction for the
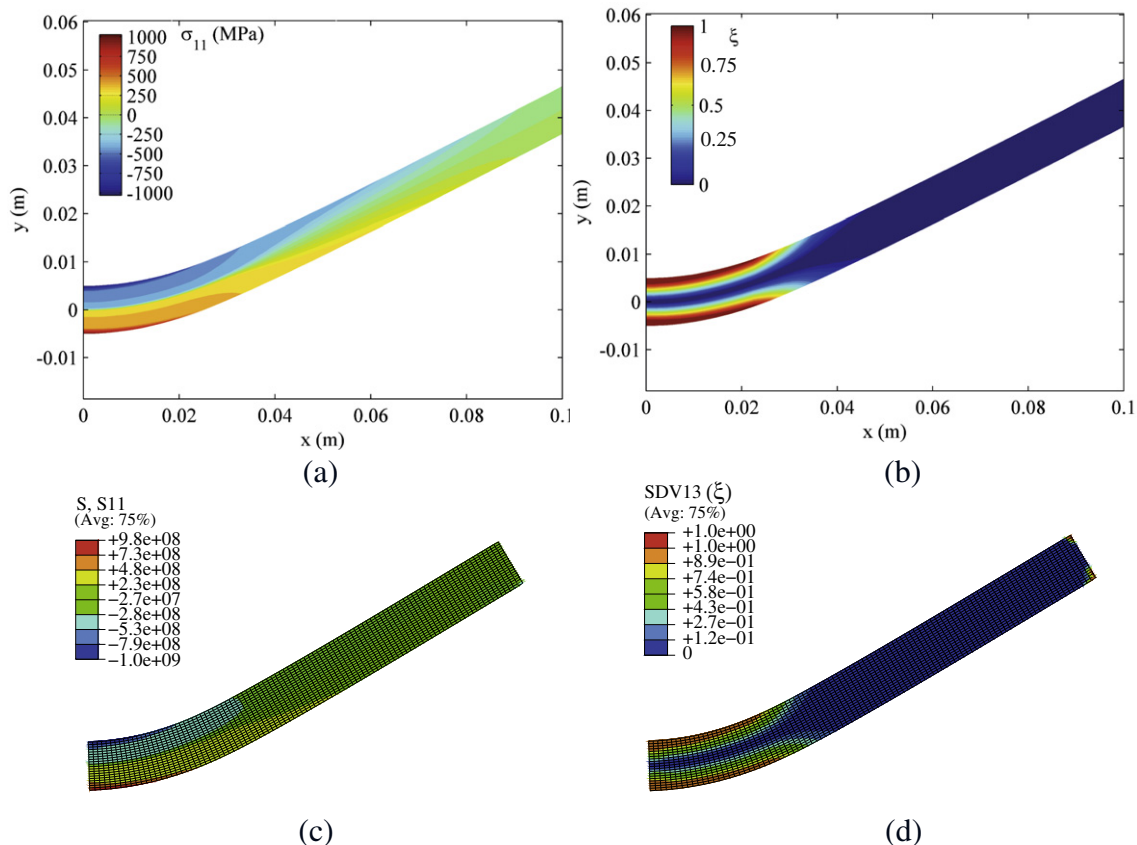

(a)

(b)

(c)

(d)

Fig. 5. Contour plots of the normal stress (a and c) and the martensitic volume fraction distributions (b and d) obtained by the analytical solution (a and b), and the finite element solution (c and d) for a beam with rectangular cross section subjected to bending. The results correspond to the end of the loading phase (see Fig. 3).
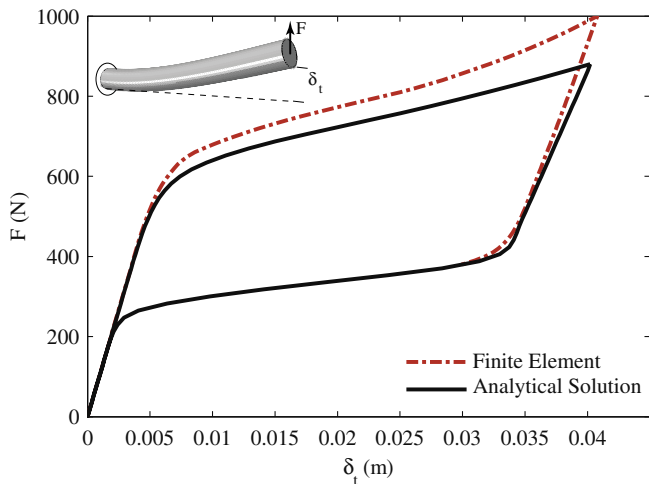
Fig. 6. Force versus tip deflection for an SMA beam with circular cross section ($R = 5$ mm, and $L = 10$ cm).

stress–strain response in uniaxial loading is compared with the experimental data in Fig. 14. It is worth noting that the experimentally observed difference in the Young modulus in tension and compression is ignored in our solution. The difference of elastic modulus in tension and compression has been reported in Plietsch and Ehrlich (1997) without explaining its origin. Frick et al. (2004) used various experimental results and asserted that the asymmetry of the tensile and compressive response of the elastic modulus is caused by strain contributions related to the transformation, such as martensite interface motion, or pre-martensitic deformation modes such as the R-phase. These strain contributions are strongly affected by the texture of a polycrystalline SMA and a micromechanical model can be used to capture such effects, while phenomenological models ignore this asymmetry. Also, the smooth hardening observed at the end of stress–strain plateau can be simulated in phenomenological models by using higher degree polynomials or trigonometric hardening functions (Lagoudas, 2008). We have chosen the quadratic function (2), which ignores this effect, for obtaining a closed-form solution.

A transverse load $F = 210$ N is applied to the superelastic cantilever (see Fig. 3 for the geometry and loading). The martensitic volume fraction distribution in the cross section near the clamped edge is shown in Fig. 15(a). Comparing this distribution with the

results in the previous case study given in Fig. 13(a), it is seen that for the material with the larger asymmetry, the neutral axis position moves further into the compression region, and the martensitic volume fraction distribution is considerably asymmetric with respect to the centerline. The stress distribution in the cross section near the clamped edge of a beam made of this material with large tension–compression asymmetry is shown in Fig. 15(b). As it is seen, the compression part is considerably smaller than the tension region. This is expected from the stress–strain response shown in Fig. 14. The large asymmetry in the stress and martensitic volume fraction distributions clearly shows that using a symmetric constitutive model for this case leads to erroneous results. Our model is stable in modeling the bending of superelastic SMA beams made of materials with large asymmetries in tensile and compressive responses.

4.5. Three-point bending test of a NiTi beam

A NiTi shape memory alloy beam is used to compare the experimental and the corresponding theoretical results. A schematic of the setup for performing the three-point bending test is shown in Fig. 16. The length of the SMA beam is $L = 170$ mm and the cross section is rectangular with $w = 7.5$ mm and $h = 3$ mm. The SMA beam is made of a nearly equiatomic NiTi alloy and the material properties of $Ni_{50}Ti_{50}$ (Jacobus et al., 1996) as mentioned in Section 4.1 are used for developing the analytic solution. It is worth noting that thermal treatments and deformation processing may change the material properties slightly. However, in this case by performing a simple tension test on the sample, it was observed that using the same material properties predicts the response in tension with an acceptable accuracy (see Mirzaeifar et al. (2011b) for some examples of comparing the response of SMA samples in uniaxial tests with the results predicted by the present constitutive equations). A 250 kN MTS Universal Testing Machine is used for performing the three-point bending test with the setup shown in Fig. 16. The maximum deflection of the center is set to $\delta = 20$ mm and the loading–unloading is performed slowly to ensure the isothermal condition.

The non-dimensional load–deflection response of the beam obtained from the experiment is compared with the theoretical results in Fig. 17. As it is shown in this figure, the loading response is accurately predicted by the $J_2 - I_1$-based model. However, the results in the unloading phase show a larger difference. This is because the constitutive equations used in this work (with the choice of polynomial hardening function) cannot predict the smooth stress–strain plateau in unloading and this difference is
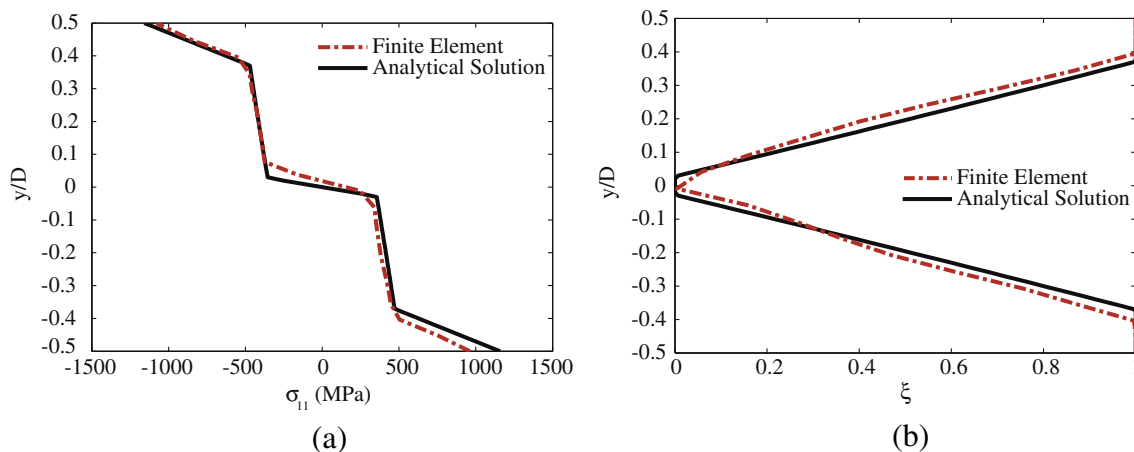

Fig. 7. Comparison of the finite element and analytical results for (a) normal stress and (b) martensitic volume fraction distribution at the clamped edge of an SMA beam with circular cross section subjected to bending. The results correspond to the end of the loading phase (see Fig. 6).
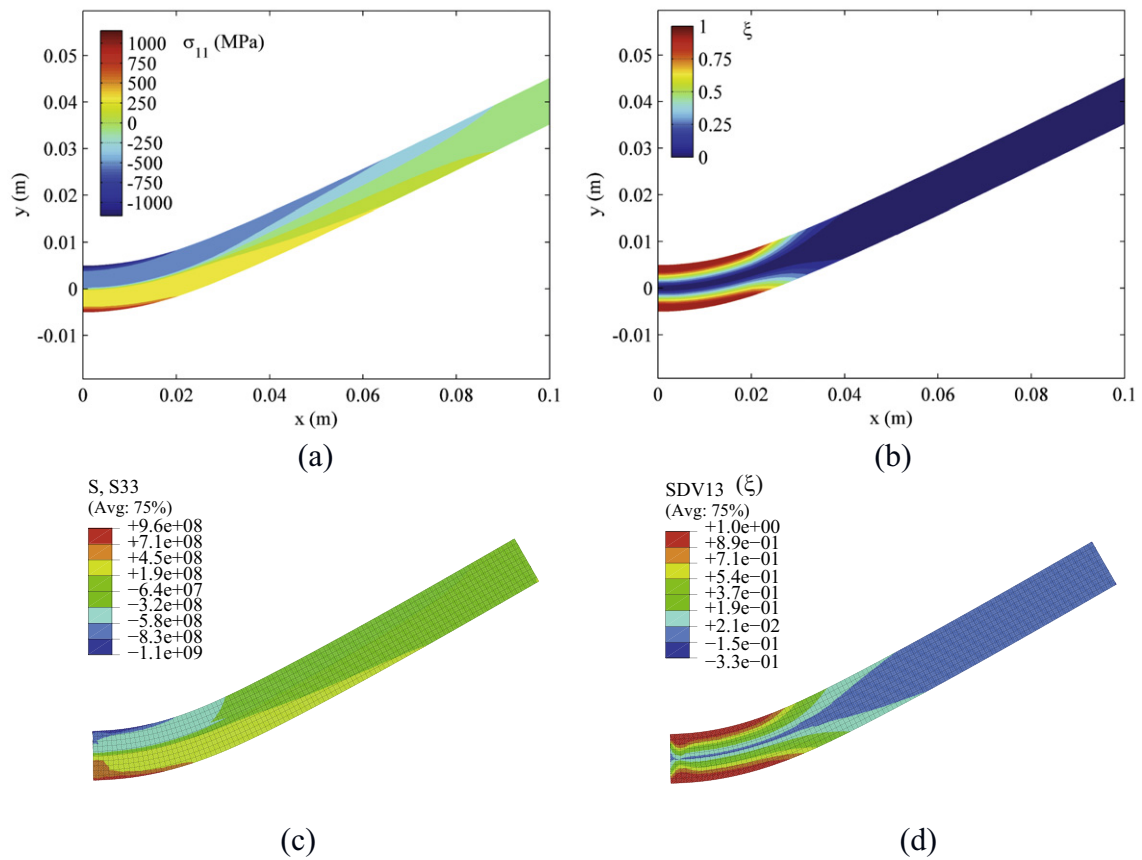
Fig. 8. Contour plots of the normal stress (a and c) and the martensitic volume fraction distributions (b and d) obtained by the analytical solution (a and b), and the finite element solution (c and d) for a beam with circular cross section subjected to bending. The results correspond to the end of the loading phase (see Fig. 6).
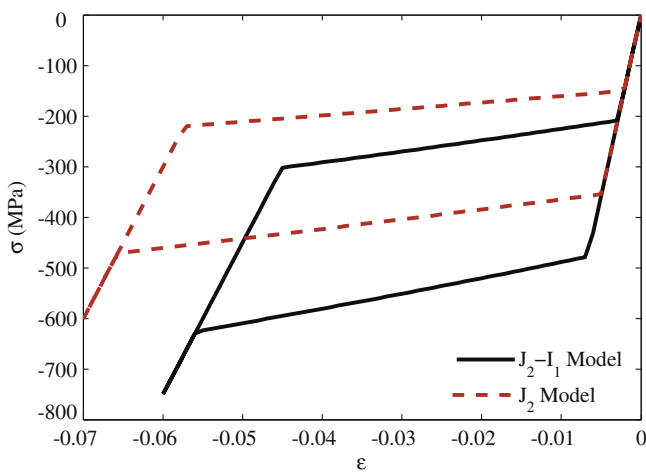

Fig. 9. Axial stress versus axial strain for J_2 and J_2-I_1 transformation functions under uniaxial compression loading–unloading.

Fig. 10. Comparison of the force-tip deflection response for an SMA beam calculated by the J_2 and J_2-I_1 based models. Two different cases of equal tip deflection and equal applied force are presented (the cross section is rectangular with $b = 1.5$ mm, $h = 1$ cm, and $L = 10$ cm).

more when unloading starts before the material is fully transformed to martensite ($\xi < 1$). In the presented test, the thickness of the SMA beam is small and the phase transformation is not completed in most parts of the cross section (see the previous sections for some examples of SMA beams with larger thicknesses). By increasing the thickness, the error in the unloading phase is decreased remarkably. It is worth noting that by modifying the hardening function (2) the constitutive equation results improve in the unloading phase (Lagoudas, 2008). However, more complicated

hardening functions are not suitable for developing closed-form solutions.

4.6. Bending of micropillars

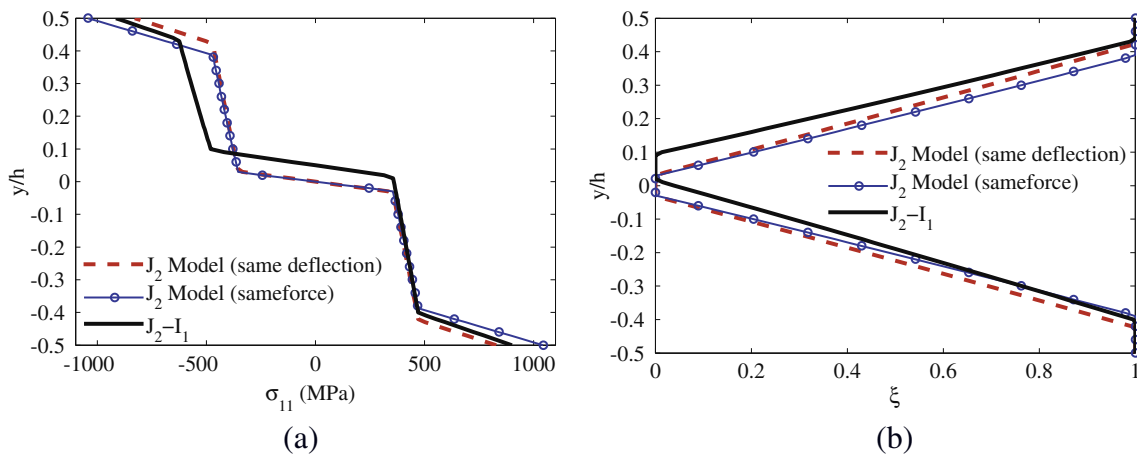As was mentioned earlier, one application of our analytic solution is the assessment of material properties in tension

Fig. 11. Comparison of the J_2 and J_2-I_1-based model results for (a) normal stress and (b) martensitic volume fraction distribution at the clamped edge of an SMA beam with rectangular cross section subjected to bending. Two different cases of equal tip deflection and equal applied force are presented. The results correspond to the end of the loading phase (see Fig. 10).
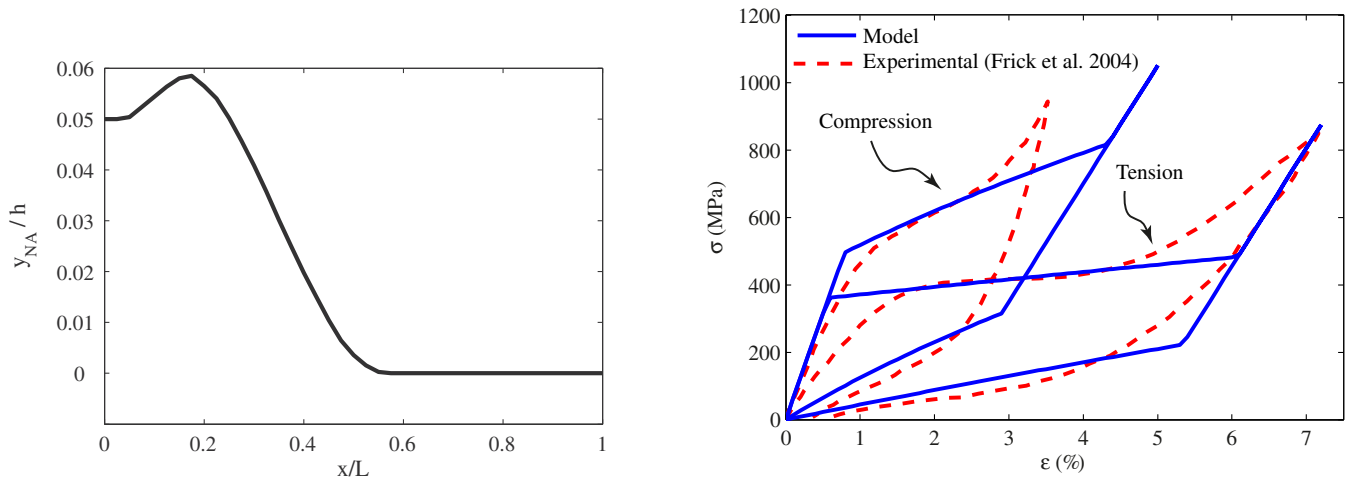

Fig. 12. The location of the neutral axis with respect to the cross section centroid along the length of an SMA beam in bending.

Fig. 14. The stress–strain response in uniaxial loading for a cast, hot rolled, then cold drawn polycrystalline NiTi with a large tension–compression asymmetry (Frick et al., 2004).

(compression) when the bending and compressive (tensile) responses are known but performing tension (compression) tests is practically difficult. Our solution is developed based on the constitutive equations suitable for polycrystalline SMAs, and an example of such application for polycrystalline SMAs is to obtain the compressive response of tiny wires using the known bending and
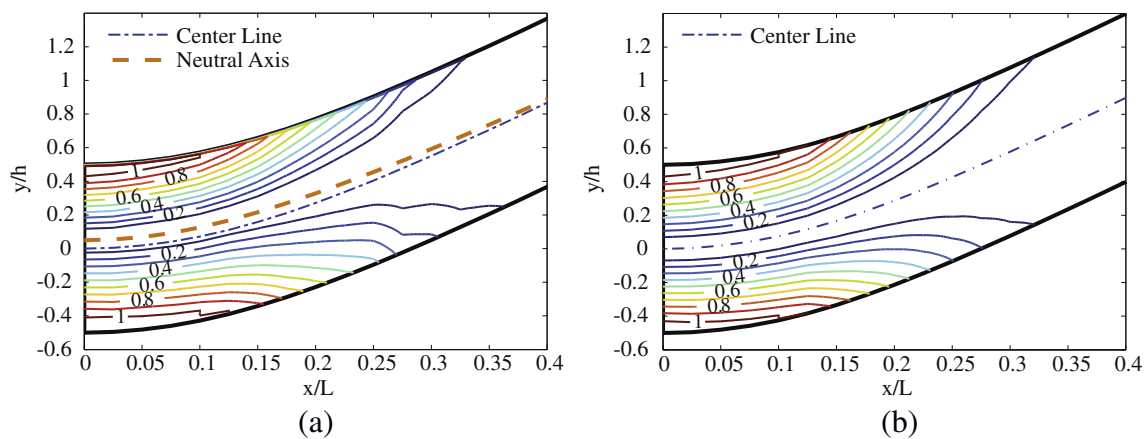

Fig. 13. Contour plots of the martensitic volume fraction distribution near the clamped edge obtained by (a)J_2-I_1 and (b)J_2 models for a beam with rectangular cross section subjected to bending. The results are for the equal tip deflection at the end of loading phase (see Fig. 10).
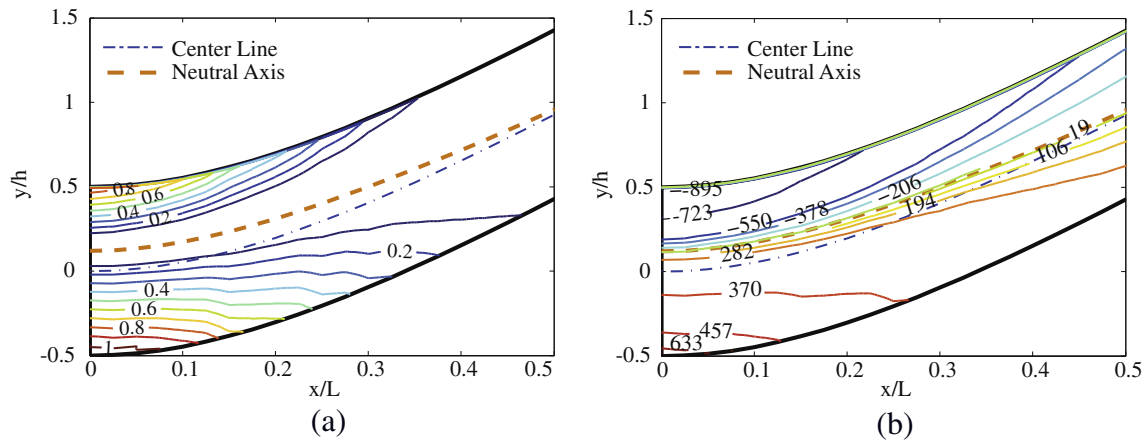
Fig. 15. Contour plots of (a) the martensitic volume fraction distribution, and (b) the stress distribution near the clamped edge for a material with large tension-compression asymmetry (see Fig. 14).
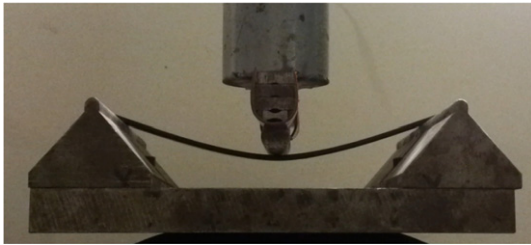

Fig. 16. The experimental setup for the three-point bending test of an SMA beam.

Fig. 17. Comparison of the non-dimensional load–deflection response obtained from three-point bending test and theoretical solutions.

tensile test results. However, we will consider a different example in this section. Although the constitutive equations of this paper are developed for modeling polycrystalline SMAs, we will show that the analytical solution of this paper can also be used as an approximation for studying the single crystal NiTi micropillars with specific orientations with a significant hardening in the stress–strain response.

In this section we study the superelastic response of NiTi microscale pillars. Nickel-titanium nano to micro scale pillars have been extensively studied experimentally in recent years. In experiments on compressive loading of micropillars, it is observed that the [1 1 1] NiTi samples exhibit a significant hardening during phase transformation compared to [1 0 0] oriented samples (compare the stress–strain curves for [1 0 0] oriented crystals in Juan et al. (2008, 2009) with the response of [1 1 1] crystals in Manjeri et al. (2010) and Frick et al. (2007)). This phenomenon is expected from the theory as well because the NiTi crystals of [1 1 1] orientation are hard under compression (Gall et al., 1999a). The hardening during phase transformation in the compressive response of [1 1 1] NiTi micropillars motivated us to implement the present formulation, which is capable of considering the stress hardening with arbitrary slope in the phase transformation plateau[3] (see Fig. 9) for studying bending of micropillars. We show in this section that the material properties predicted by this method are in good agreement with the expected properties for NiTi single crystals as well. The experimental results on the bending of a micropillar reported by Clark et al. (2010) are used in this section. They tested a [1 1 1] oriented NiTi pillar with a diameter of $D_t = 1.2$ μm at the
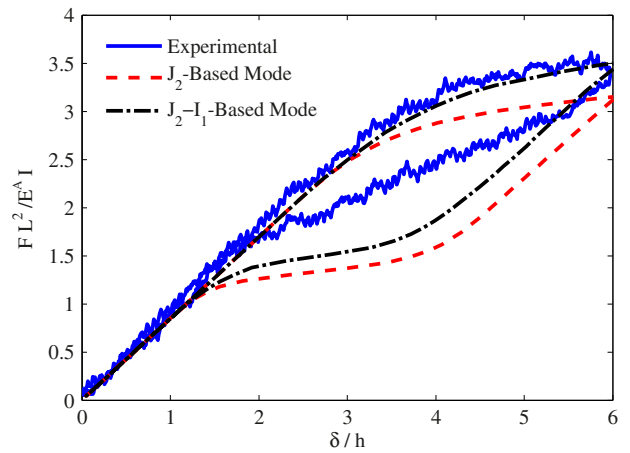
---

[3] The slope of stress–strain plateau for single crystal SMAs in some specific orientations and also polycrystalline SMAs with particular heat treatments may be near zero. The material properties of the presented model cannot be calibrated for modeling a zero slope during the transformation. However, these properties can be calibrated for modeling a very small slope in the stress–strain plateau if needed.
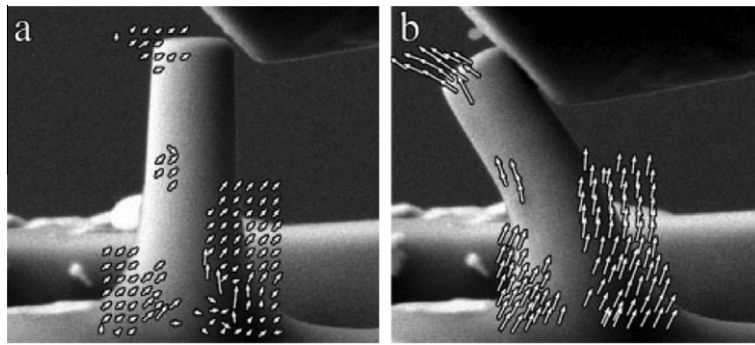
top of pillar and length of $L = 3.8$ μm. The undeformed micropillar and the deformed shape of the micropillar subjected to bending are shown in Fig. 18. As mentioned in the pillar specifications, all the samples had an estimated taper angle of ≈3°–5°. We consider a 3° angle, which leads to a diameter of $D_t = 1.6$ μm at the pillar base.

Among the material properties required for our constitutive model, the austenite finish temperature is reported as $A_f = 33\ °C$. The other properties in compression can be calibrated by using a cyclic compressive test on the micropillar reported in (Clark et al., 2010). These properties are obtained as follows (some of the properties are considered identical with those of the NiTi bulk material as given in the previous sections): $E^A = 55$ MPa, $E^M = 50$ MPa, $v^A = v^M = 0.3$, $\rho c^A = \rho c^M = 2.6 \times 10^6$ J/(m^3 K), $H^t = 0.05$, $H^c = -0.03$, $(d\sigma/dT)^A_t = 11.4 \times 10^6$ J/(m^3 K), $\rho \Delta s_0 = -H^t(d\sigma/dT)^A_t = -0.57 \times 10^6$ J/(m^3 K), $A_f = 306$ K, $A_s = 4288$ K, $M_f = 242$ K, $M_s = 274K$. We use the J_2–I_1-based model for analyzing this case study by setting $\hat{\eta} = \eta = \frac{1}{2}(H^t + |H^c|)$, and $\hat{\omega} = \omega = \frac{1}{2}(H^t - |H^c|)$. It is worth noting that for calibrating these properties, H_t, and $(d\sigma/dT)^A_t$ cannot be obtained only from the compression test; we have used an error and trial method for finding these properties for the best match in the theoretical and experimental results in bending as it will be discussed shortly. The material response in compression obtained from the experiments (Clark et al., 2010) and the present model are

Fig. 18. SEM images showing (a) the initial configuration and the inclined flat-tip punch, and (b) in situ bending of the pillar. Copyright (2010) Wiley. Used with publisher permission from Clark et al. (2010), Wiley.
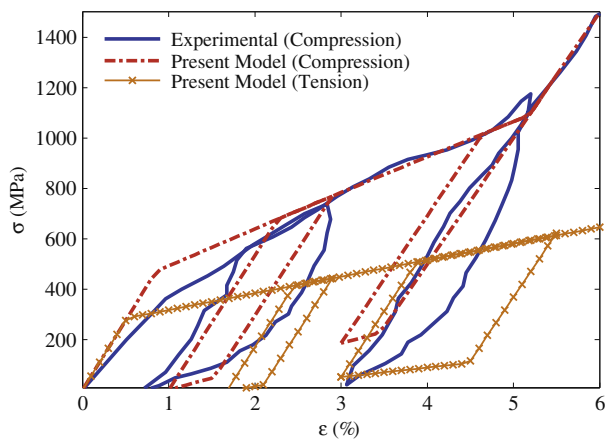

Fig. 19. The compressive stress–strain response of [111] NiTi micro pillars obtained from experiments (Clark et al., 2010), and the compressive and tensile response obtained from the present model.
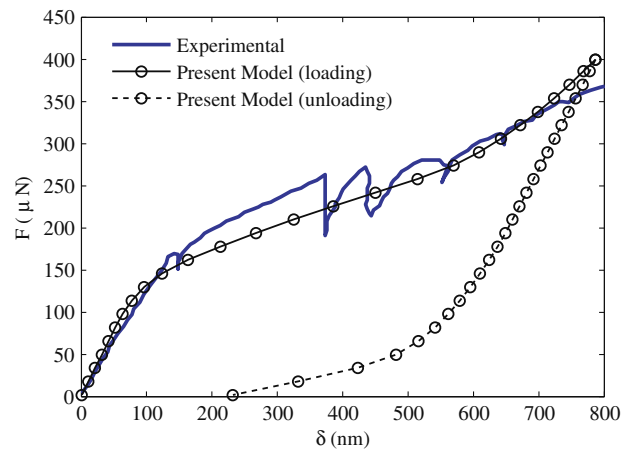

Fig. 20. Comparison of the force–deflection response for micropillars obtained from experiments (Clark et al., 2010) and the present formulation.

compared in Fig. 19 for two loading–unloading cycles with 3% and 5% axial strains.[4]

The pillar is subjected to bending using an inclined indenter with the angle of $\approx 60°$ (see Fig. 18). As mentioned in (Clark et al., 2010), the pillar slips on the indenter during loading and this releases the axial compressive load. It can be assumed that the pillar is subjected to a pure bending with the projection of force in the transverse direction.[5] The transverse force versus tip deflection obtained from the present formulation with the J_2-I_1-based model is compared with the experimental results in Fig. 20. As it is shown, the present model predicts the force-deflection in bending of the micropillar with a good accuracy. It is worth noting that the experiment contains loading further up to a tip deflection of near 1500 nm. However, as it is shown in Fig. 20 for tip deflections larger than $\delta \approx 790$ nm the force-deflection slope suddenly decreases (see Fig. 2(e) in (Clark et al., 2010)). This is due to the start of plastic deformation of martensite that happens by further loading the material far beyond the completion of phase transformation. We are not

considering the martensite plastic response in our model and restrict our comparison to the start of the plastic deformation. The dashed line in Fig. 20 shows the model prediction for the unloading phase if the pillar was unloaded after the maximum tip deflection of $\delta \approx 790$ nm. As it is shown, even by ignoring the plastic nonrecoverable response a residual deflection is observed in the model. This is due to the ambient temperature $T = 300$ K, which is slightly bellow A_f temperature.

The present method can be used to calculate the stress distribution and the intensity of phase transformation inside and at the surface of the micropillar (which are both extremely difficult to be measured experimentally). The martensitic volume fraction distribution, as a measure of the phase transformation intensity, is shown in Fig. 21(a), and the stress distribution at the surface at the end of the loading phase is shown in Fig. 21(b). As it is shown in Fig. 21(b), the maximum stress at the surface is ≈ 2500 MPa. This is in agreement with our previous prediction of martensite plastic deformation start at this tip deflection. The reason is that the compression tests show the same stress for the start of martensite plastic deformation (see Fig. 4 in (Clark et al., 2010)). Considering the fact that the present model with the calibrated material properties is predicting the material response in both compression and bending with good accuracy, it can be concluded that the material properties in tension are also assumed accurately (these properties are guessed by considering the bending results for finding the best possible match). The predicted

---

[4] In the compression response reported in (Clark et al., 2010), the initiation of loading was associated with a stress–strain plateau with a very small slope. It was assumed that the small Young modulus at the start of loading is due to the imperfect contact. We calibrated the austenite elastic modulus by ignoring the initial low elastic modulus in the response. This region is not shown in Fig. 19 for the sake of clarity.

[5] The transverse force is $F = F_a \cos(60°) = 0.5F_a$, where F_a is the actuation force reported in (Clark et al., 2010), and $60°$ represents the indenter angle (see Fig. 1(b) in (Clark et al., 2010)).
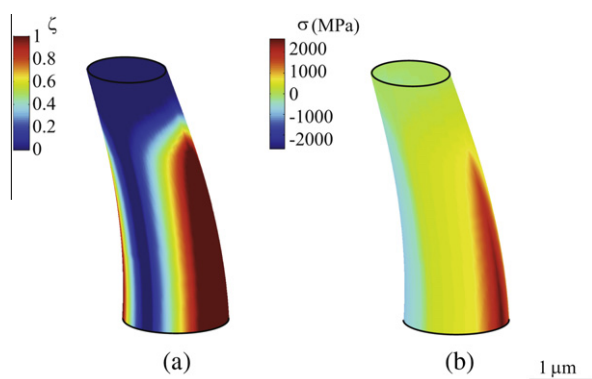
Fig. 21. Distributions of (a) phase transformation intensity, and (b) stress at the surface of a micropillar subjected to bending obtained from the present closed-form solution.

material response in tension for two loading–unloading cycles with 3% and 5% tensile strains is also shown in Fig. 19. The predicted response in tension for this special geometry is valuable because it is practically very difficult to test a micropillar in tension. It is worth noting that there are several uncertainties in the experiment used in this section, including the non-uniform cross section of the pillar, the inclined indentor for bending, and the imperfect contact at the start of compressive loading that cause the observed error in the results. In order to obtain more accurate results, a specific experiment on a micropillar with uniform cross section subjected to bending with a sharp perpendicular indentor is required. Also, various length to thickness ratios should be considered for studying the effect of shear deformation on the bending response of NiTi micropillars. However, as it will be shown in the following, the results of this section are in agreement with the theoretical expectations for single crystal NiTi shape memory alloys.

The predicted maximum transformation strains in tension and compression are in agreement with the response of [1 1 1] oriented NiTi single crystals. Considering the crystallographic data for 24 martensite correspondence variant pairs (CVPs) in NiTi (see Table 1 in (Gall et al., 1999a)), and using the method described in detail by Gall et al., 1999a, it can be shown that for a [1 1 1] oriented NiTi single crystal, CVP#2 with habit plane normal $\mathbf{n} = (-0.4044, -0.8889, -0.2152)$ and transformation direction $\mathbf{m} = (-0.4981, 0.4114, -0.7633)$ is the first CVP to satisfy the transformation criteria in tension, and the CVP#1 with habit plane normal $\mathbf{n} = (-0.8889, -0.4044, 0.2152)$ and transformation direction $\mathbf{m} = (0.4114, -0.4981, 0.7633)$ is the first CVP to satisfy the transformation criteria in compression. Using these directions and the magnitude of transformation $g = 0.13078$, the transformation strain for the kth variant is given by $\epsilon_{ij}^k = \frac{g}{2}(m_i^k n_j^k + m_j^k n_i^k)$ (Gall et al., 1999a). Calculating the transformation strain tensors for tension and compression with the given directions, the normal transformation strains in [1 1 1] direction are obtained as $\epsilon_t^t = 5.59\%$ and $\epsilon_c^t = 3.18\%$ in tension and compression, respectively. These transformation strains are in good agreement with the values obtained for $H_t = 5\%$ and $H_c = 3\%$ that represent the maximum transformation strains in our model. Using the transformation criteria for NiTi single crystals given in (Gall et al., 1999a), the ratio of phase transformation start stresses in tension and compression is given by $|\hat{\sigma}_c|/\hat{\sigma}_t = \hat{\alpha}_t/|\hat{\alpha}_c|$, where $\hat{\sigma}$ is the critical stress at which phase transformation starts and $\hat{\alpha}$ is the normal component of the tensor $\boldsymbol{\alpha}$ on (1 1 1) plane with $\alpha_{ij} = \frac{1}{2}(m_i^k n_j^k + m_j^k n_i^k)$. This ratio is obtained as $|\hat{\sigma}_c|/\hat{\sigma}_t = 1.7578$ using the $\mathbf{m}$ and $\mathbf{n}$ directions given above, which is in agreement with the value predicted by our model $|\hat{\sigma}_c|/\hat{\sigma}_t = 477/275 = 1.7345$ (see Fig. 19).

5. Conclusions

In this paper a closed-form solution is given for bending analysis of superelastic shape memory alloy beams. Some three-dimensional constitutive relations are reduced to an appropriate one-dimensional form required for formulating the bending problem and explicit expressions are given for the stress and martensitic volume fraction distributions in the beam cross section. These explicit expressions are used for obtaining closed-form relations between bending moment and curvature in pure bending. In addition to a model based on symmetric tension–compression response, another method is presented that is capable of modeling bending in materials that have asymmetric response in tension and compression. Several case studies are presented for studying the accuracy of our method by comparing the results with those of three-dimensional finite element simulations. The effect of taking into account the tension–compression asymmetry in the bending response of shape memory alloys is also studied. In order to study the applicability of the present formulation in the micro scale, some experimental data on the bending of a [1 1 1] oriented NiTi micropillar are used. It is shown that the present formulation can be used for calculating the global force–deflection response with a good accuracy compared to the experimental results. Our model is shown to be very useful in finding the stress distributions, which are practically difficult to be measured in experiments. It is also shown that the present formulation can be used to find the tensile response of micropillars (which is very difficult to be measured experimentally) by using the responses in compression and bending. The predicted tensile response is compared with those obtained from analyzing [1 1 1] oriented NiTi single crystals, and a good agreement is observed.

Studying the large strain effects in bending analysis of SMA superelastic beams is an important extension of the present work, which can be obtained using the approximation III. This approximation can also be used for developing a closed-form solution based on higher-order beam theories. Adding the thermo-mechanical coupling effect to the present model enables it to consider the phase transformation latent heat effect on the bending of SMA beams, which leads to a comprehensive solution capable of modeling the rate dependency, ambient condition effects, and size effect in the response of superelastic SMA beams in bending. These will be the subjects of future communications.

References

Abramowitz, M., Stegun, I.A., 1964. Handbook of Mathematical Functions with Formulas, Graphs and Mathematical Tables. National Bureau of Standards Applied Mathematics, Washington.

Anand, L., Gurtin, M.E., 2003. Thermal effects in the superelasticity of crystalline shape-memory materials. Journal of the Mechanics and Physics of Solids 51 (6), 1015–1058.

Atanackovic, T., Achenbach, M., 1989. Moment-curvature relations for a pseudoelastic beam. Continuum Mechanics and Thermodynamics 1, 73–80.

Auricchio, F., Sacco, E., 1999. A temperature-dependent beam for shape-memory alloys: constitutive modelling, finite-element implementation and numerical simulations. Computer Methods in Applied Mechanics and Engineering 174, 171–190.

Auricchio, F., Sacco, E., 2001. Thermo-mechanical modelling of a superelastic shape-memory wire under cyclic stretching–bending loadings. International Journal of Solids and Structures 38 (34–35), 6123–6145.

Auricchio, F., Taylor, R.L., Lubliner, J., 1997. Shape-memory alloys: macromodelling and numerical simulations of the superelastic behavior. Computer Methods in Applied Mechanics and Engineering 146, 281–312.

Auricchio, F., Reali, A., Stefanelli, U., 2009. A macroscopic 1D model for shape memory alloys including asymmetric behaviors and transformation-dependent

elastic properties. Computer Methods in Applied Mechanics and Engineering 198 (17–20), 1631–1637.

Auricchio, F., Morganti, S., Reali, A., Urbano, M., 2011. Theoretical and experimental study of the shape memory effect of beams in bending conditions. Journal of Materials Engineering and Performance 20 (4–5), 712–718.

Bhattacharya, K., James, R., 2005. The material is the machine. Science 307 (5706), 53–54.

Bo, Z., Lagoudas, D.C., 1999. Thermomechanical modeling of polycrystalline smas under cyclic loading, Part I: Theoretical derivations. International Journal of Engineering Science 37 (9), 1089–1140.

Boyd, J.G., Lagoudas, D.C., 1996. Thermodynamical constitutive model for shape memory materials. Part I. The monolithic shape memory alloy. International Journal of Plasticity 12 (6), 805–842.

Clark, B.G., Gianola, D.S., Kraft, O., Frick, C.P., 2010. Size independent shape memory behavior of nickel–titanium. Advanced Engineering Materials 12 (8), 808–815.

Flor, D.L.S., Urbina, C., Ferrando, F., 2011. Asymmetrical bending model for niti shape memory wires: numerical simulations and experimental analysis. Strain 47 (3), 255–267.

Forsythe, G.E., Malcolm, M.A., Moler, C.B., 1976. Computer Methods for Mathematical Computations. Prentice-Hall.

Frick, C.P., Ortega, A.M., Tyber, J., Gall, K., Maier, H.J., 2004. Multiscale structure and properties of cast and deformation processed polycrystalline niti shape-memory alloys. Metallurgical and Materials Transactions A: Physical Metallurgy and Materials Science 35 A (7), 2013–2025.

Frick, C., Orso, S., Arzt, E., 2007. Loss of pseudoelasticity in nickel–titanium sub-micron compression pillars. Acta Materialia 55 (11), 3845–3855.

Gall, K., Sehitoglu, H., 1999a. The role of texture in tension–compression asymmetry in polycrystalline NiTi. International Journal of Plasticity 15 (1), 69–92.

Gall, K., Sehitoglu, H., Chumlyakov, Y., Kireeva, I., 1999b. Tension–compression asymmetry of the stress–strain response in aged single crystal and polycrystalline NiTi. Acta Materialia 47 (4), 1203–1217.

Gall, K., Sehitoglu, H., Anderson, R., Karaman, I., Chumlyakov, Y.I., Kireeva, I.V., 2001. On the mechanical behavior of single crystal NiTi shape memory alloys and related polycrystalline phenomenon. Materials Science and Engineering A 317 (1–2), 85–92.

Gillet, Y., Patoor, E., Berveiller, M., 1998. Calculation of pseudoelastic elements using a non-symmetrical thermomechanical transformation criterion and associated rule. Journal of Intelligent Material Systems and Structures 9, 366–378.

Jacobus, K., Sehitoglu, H., Balzer, M., 1996. Effect of stress state on the stress-induced martensitic transformation in polycrystalline Ni-Ti alloy. Metallurgical and Materials Transactions A 27, 3066–3073.

Juan, J.S., No, M.L., Schuh, C.A., 2009. Nanoscale shape-memory alloys for ultrahigh mechanical damping. Nature Nanotechnology 4 (7), 415–419.

Kahn, H., Huff, M.A., Heuer, A.H., 1998. The TiNi shape-memory alloy and its applications for MEMS. Journal of Micromechanics and Microengineering 8 (3), 213–221.

Kim, J.-Y., Greer, J.R., 2009. Tensile and compressive behavior of gold and molybdenum single crystals at the nano-scale. Acta Materialia 57 (17), 5245–5253.

Kim, J.-Y., Jang, D., Greer, J.R., 2009. Insight into the deformation behavior of niobium single crystals under uniaxial compression and tension at the nanoscale. Scripta Materialia 61 (3), 300–303.

Krulevitch, P., Lee, A., Ramsey, P., Trevino, J., Hamilton, J., Northrup, M., 1996. Thin film shape memory alloy microactuators. Journal of Microelectromechanical Systems 5 (4), 270–282.

Lagoudas, D.C., 2008. Shape Memory Alloys: Modeling and Engineering Applications. Springer, New York.

Liu, Y., Xie, Z., Humbeeck, J.V., Delaey, L., 1998. Asymmetry of stress–strain curves under tension and compression for niti shape memory alloys. Acta Materialia 46 (12), 4325–4338.

Manjeri, R.M., Qiu, S., Mara, N., Misra, A., Vaidyanathan, R., 2010. Superelastic response of [1 1 1] and [1 0 1] oriented niti micropillars. Journal of Applied Physics 108 (2), 023501.

Marfia, S., Sacco, E., Reddy, J.N., 2003. Superelastic and shape memory effects in laminated shape-memory-alloy beams. AIAA Journal 41 (1), 100–109.

Mirzaeifar, R., Shakeri, M., Sadighi, M., 2009. Nonlinear finite element formulation for analyzing shape memory alloy cylindrical panels. Smart Materials and Structures 18 (3), 035002.

Mirzaeifar, R., Desroches, R., Yavari, A., 2010. Exact solutions for pure torsion of shape memory alloy circular bars. Mechanics of Materials 42 (8), 797–806.

Mirzaeifar, R., Desroches, R., Yavari, A., 2011a. Analysis of the rate-dependent coupled thermo-mechanical response of shape memory alloy bars and wires in tension. Continuum Mechanics and Thermodynamics 23 (4), 363–385.

Mirzaeifar, R., Desroches, R., Yavari, A., 2011b. A combined analytical, numerical, and experimental study of shape-memory-alloy helical springs. International Journal of Solids and Structures 48 (3–4), 611–624.

Mirzaeifar, R., Shakeri, M., DesRoches, R., Yavari, A., 2011c. A semi-analytic analysis of shape memory alloy thick-walled cylinders under internal pressure. Archive of Applied Mechanics 81 (8), 1093–1116.

Paiva, A., Savi, M.A., Braga, A.M.B., Pacheco, P.M.C.L., 2005. A constitutive model for shape memory alloys considering tensile-compressive asymmetry and plasticity. International Journal of Solids and Structures 42 (11–12), 3439–3457.

Patoor, E., Elamrani, M., Eberhardt, A., Berveiller, M., 1995. Determination of the origin for the dissymmetry observed between tensile and compression tests on shape-memory alloys. Journal De Physique IV 5 (C2), 495–500.

Plietsch, R., Ehrlich, K., 1997. Strength differential effect in pseudoelastic NiTi shape memory alloys. Acta Materialia 45 (6), 2417–2424.

Plietsch, R., Bourauel, C., Drescher, D., Nellen, B., 1994. Analytical description of the bending behaviour of niti shape-memory alloys. Journal of Materials Science 29 (22), 5892–5902.

Purohit, P.K., Bhattacharya, K., 2002. On beams made of a phase-transforming material. International Journal of Solids and Structures 39 (13–14), 3907–3929.

Qidwai, M.A., Lagoudas, D.C., 2000a. Numerical implementation of a shape memory alloy thermomechanical constitutive model using return mapping algorithms. International Journal for Numerical Methods in Engineering 47 (6), 1123–1168.

Qidwai, M.A., Lagoudas, D.C., 2000b. On thermomechanics and transformation surfaces of polycrystalline NiTi shape memory alloy material. International Journal of Plasticity 16 (10), 1309–1343.

San Juan, J.M., No, M.L., Schuh, C.A., 2008. Superelasticity and shape memory in micro- and nanometer-scale pillars. Advanced Materials 20 (2), 272–278.

Shin, D.D., Mohanchandra, K.P., Carman, G.P., 2005. Development of hydraulic linear actuator using thin film sma. Sensors and Actuators A: Physical 119 (1), 151–156.

Thamburaja, P., Anand, L., 2001. Polycrystalline shape-memory materials: effect of crystallographic texture. Journal of the Mechanics and Physics of Solids 49 (4), 709–737.

Thamburaja, P., Anand, L., 2002. Superelastic behavior in tension–torsion of an initially-textured Ti–Ni shape-memory alloy. International Journal of Plasticity 18 (11), 1607–1617.

Volkert, C.A., Minor, A.M., 2007. Focused ion beam microscopy and micromachining. MRS Bulletin 32 (5), 389–395.